Research Square

Preprints are preliminary reports that have not undergone peer review.
They should not be considered conclusive, used to inform clinical practice,
or referenced by the media as validated information.

Thermal and Structural Effects of Calcium in Borophosphate Bioactive Glasses

Gailan A. Saber
Salahaddin University-Erbil
Saman Mawlud
saman.mawlud@su.edu.krd
Salahaddin University-Erbil

Research Article

Keywords: Physical Parameter, Glass structure, Optical band gap, FTIR, UV-Vis-NIR spectroscopy, DSC/TGA

Posted Date: March 12th, 2026

DOI: https://doi.org/10.21203/rs.3.rs-8942208/v1

License: This work is licensed under a Creative Commons Attribution 4.0 International License.
Read Full License

Additional Declarations: No competing interests reported.

Version of Record: A version of this preprint was published at Journal of Thermal Analysis and Calorimetry on May 9th, 2026. See the published version at https://doi.org/10.1007/s10973-026-15579-0.

Thermal and Structural Effects of Calcium in Borophosphate Bioactive Glasses

Gailan A. Saber[1] and Saman Q. Mawlud[*1]
[1]Department of Physics, College of Education, Salahaddin University-Erbil, Erbil, Iraq
*Corresponding author: saman.mawlud@su.edu.krd

Abstract:
A series of borophosphate glasses with the composition (65-x) B_2O_3 + 15 P_2O_5 + 20 Na_2O + x CaO (x = 0, 2.5, 5, 7.5, 10, and 15 mol%) synthesized by melt-quenching technique. XRD analysis confirmed the amorphous nature of the glass. FTIR spectroscopy used to investigate structural changes in the borophosphate glass with varying CaO content. In BPNC0 sample, bands were observed between 500–650 cm^{-1} (B-O-B), 1050 cm^{-1} (P-O-P), 1465–1471 cm^{-1} (H-O-H), and 3215–3446 cm^{-1} (O-H). With CaO incorporation, notable shifts and new bands emerged. Broader bands from 400–1600 cm^{-1} in higher CaO contents indicated the presence of metallic bonds, network depolymerization and structural rearrangements confirming the role of CaO as a network modifier. Physical parameters systematically evaluated, revealing a densification trend with increasing CaO content. Density fluctuated between 2.163 to 2.532 g/cm^3, while molar volume fluctuated between 46.34 to 39.05 cm^3/mol, indicating tighter atomic packing. OPD fluctuated from 69.73 to 62.58 mol/L, suggesting enhanced structural compactness. Optical absorption spectra analyzed via the UV-Vis-NIR spectrometer, the Urbach rule showed a redshift in the absorption edge, with the optical band gap fluctuating from 2.470 to 3.162 eV as CaO content increased, implying the generation of non-bridging oxygen atoms and expanded conduction bands. The metallization criterion calculated from refractive index and band gap values fluctuated from 0.351 to 0.397 by increasing CaO, indicating higher metallic character; these findings point to a tunable electronic structure. The thermal stability of the glass has been determined by means of Differential Scanning Calorimetry/Thermogravimetric Analysis (DSC/TGA). From the DSC/TGA curve, the glass transition temperature (T_g), crystallization temperature (T_c) and melting temperature (T_m) have been identified and thermal stability is also calculated. The tailored compositional design significantly affects bioactivity, positioning these borophosphate glasses as promising candidates for bone regeneration.

Keywords: Physical Parameter, Glass structure, Optical band gap, FTIR, UV-Vis-NIR spectroscopy, DSC/TGA

1. Introduction

Bioactive glass (BG) is an innovative and versatile class of materials that has revolutionized the field of biomaterials since its discovery by Larry Hench in 1969 [1]. Bioactive glass represents a significant advancement in materials science, particularly within the field of biomaterials engineering. Developed initially as a silicate-based glass system, bioactive glass is engineered to elicit specific biological responses at the interface between the material and surrounding tissue. Its functionality is rooted in its composition and structure, typically consisting of SiO_2, CaO, Na_2O, and P_2O_5, with each component playing a critical role in its reactivity and degradation behavior [2] . The key to its bioactivity lies in its ability to undergo surface reactions in physiological environments, leading to the formation of a hydroxycarbonate apatite (HCA) layer that mimics the mineral phase of bone. From a materials science perspective, bioactive glass offers a unique combination of properties: it is degradable, ion-releasing, and structurally customizable, making it ideal for tailoring biological and mechanical performance. Advances in sol-gel processing, melt-quenching, and compositional tuning such as the incorporation of therapeutic ions like zinc, silver, or strontium have expanded its potential far beyond bone repair to include antimicrobial action, angiogenesis, and soft tissue regeneration [3].

Recent years have seen notable progress in enhancing (BG) for bone regeneration and beyond. Haider et al. (2020) developed alginate-based scaffolds incorporating strontium and zinc, demonstrating improved mechanical strength and in vitro osteogenic potential through ion release that promotes bone formation [4]. Zhang et al. (2019) introduced mesoporous strontium-incorporated bioactive glass (Sr-MBG), which stimulated proliferation and osteogenic differentiation of bone marrow stromal cells, and enhanced healing in osteoporotic rat femur defects [5]. Gomez-Cerezo et

al. (2021) produced 3D-printed MBG–PCL scaffolds with multiscale porosity, yielding high osteoblastic activity and promising mechanical properties suitable for load-bearing applications [6]. Moreover, comprehensive reviews, such as Balamurugam et al. (2021), have highlighted the multifunctional role of zinc-doped BGs, noting their osteogenic, angiogenic, antimicrobial, and anti-inflammatory effects, with controlled Zn release maintaining bioactivity and biocompatibility [7]. Collectively, these contemporary efforts reflect the expanding versatility of bioactive glasses ranging from therapeutic ion delivery and scaffold design to advanced fabrication techniques toward more effective and personalized bone repair strategies.

Borate-based bioactive glasses (BBGs) have emerged as a highly significant class of biomaterials, particularly valued for their accelerated degradation rates and rapid conversion to hydroxyapatite (HAp) compared to traditional silicate-based glasses. Fu et al. (2010) demonstrated that as B2O3 content increases fully replacing SiO2 in the 13-93 system the scaffolds convert to HAp significantly faster in simulated body fluid, albeit with a trade-off in mechanical strength [8, 9]. Rahaman et al. (2011) further emphasized that BBGs not only enhance new bone formation but also support angiogenesis crucial for tissue regeneration in both bone and soft tissue contexts [10] . Additionally, Brown et al. (2008) found that higher borate content accelerated HAp formation but could inhibit osteoblastic cell proliferation under static in vitro conditions, highlighting the need to balance dissolution rate with biocompatibility [9]. BBGs thus offer the advantages of customizable degradation kinetics and bioactivity, along with the capacity to incorporate therapeutic ions, although their lower mechanical robustness compared to silicate glasses necessitates careful compositional optimization. These features make borate glasses highly promising for bone regeneration, wound healing, and drug delivery applications.

Recent research has shifted attention from classic silicate-based glasses toward borate-based bioactive glasses (BBGs) due to their acceleration in vivo and in vitro behavior. Unlike traditional silicates such as the widely studied 45S5 or S53P4 systems BBGs exhibit significantly faster degradation in physiological environments and more rapid conversion into HAp, a process essential for bone bonding [11]. For example, scaffolds in the “13-93B3” borate series demonstrated nearly complete transformation into HAp and substantially faster apatite layer formation than their silicate counterparts. This speed is largely attributed to the lower chemical durability of borate networks, which also allows customizable degradation rates to match new bone growth [12]. However, this enhanced solubility can compromise mechanical stability, requiring balanced compositional tuning [11]. Additionally, BBGs lower thermal expansion coefficients and enhance coatings’ thermal compatibility with metallic implants[13]. Altogether, while silicate glasses offer structural integrity and proven clinical outcomes, borate-based compositions provide compelling benefits, namely faster bioactivity and greater compositional flexibility, making them attractive for targeted applications in bone regeneration and soft tissue engineering.

In the present study, the composition (65-x) B_2O_3+15P_2O_5+20Na_2O+xCaO is in focus which represents a borate-based bioactive glass system in which calcium oxide (CaO) content is systematically varied to study its influence on bioactivity and structural stability. This formulation is of particular interest due to the substitution of silica (SiO_2) with boron oxide (B_2O_3), which results in faster degradation rates and enhanced ion release factors beneficial for applications requiring rapid tissue regeneration. Phosphate (P_2O_5) plays a critical role in mimicking natural bone mineral composition, while Na_2O acts as a network modifier that helps control the glass dissolution rate [12]. Increasing CaO content is expected to enhance the formation of HAp on the glass surface upon immersion in simulated body fluid (SBF), improving bonding with bone tissue. However, the challenge lies in balancing degradation with sufficient mechanical integrity and biocompatibility. By tailoring the CaO content, this composition allows a systematic study of how calcium influences bioactivity, optical and structural properties. This composition is designed to investigate how incremental substitution of B_2O_3 with CaO affects the structural, physical, and optical properties of the glass. Calcium plays a critical role in bioactivity by participating in apatite formation, while boron oxide contributes to network flexibility and faster solubility. By systematically modifying the CaO content, this study aims to optimize the glass composition for potential bioactive applications, with a

particular focus on balancing degradation rate, structural integrity, and optical behavior relevant for biomedical use. In this work, a systematic investigation of calcium-modified borophosphate glass systems is presented, focusing on the combined influence of CaO incorporation on structural, thermal, physical, and optical properties. This integrated approach provides new insight into structure–property relationships and clarifies the role of CaO as a network modifier in tuning glass performance for functional applications.

2. Experimental Part

A series of borate-based bioactive glasses with the general composition (65–x) B_2O_3 + 15P_2O_5 + 20Na_2O + xCaO (mol%) were synthesized, where x = 0, 2.5, 5, 7.5, 10, and 15. High-purity reagents (all ≥99%, purchased from Sigma-Aldrich and Carl Roth) were used as raw materials: boron oxide (B_2O_3), phosphorus pentoxide (P_2O_5), sodium oxide (Na_2O), and calcium oxide (CaO). This composition range was selected to ensure meaningful structural changes induced by CaO. The chosen CaO ratio allows systematic investigation of the modifier role of Ca^{2+} ions on network depolymerization and related properties within a stable glass-forming range. The appropriate amounts of each component as presented in Table 1 were carefully weighed according to the target molar compositions and thoroughly mixed. The powder mixtures were homogenized using a rolling mixer for 15 minutes to ensure uniform distribution of the constituents. The homogenized mixture was then transferred into an alumina crucible and placed in a high-temperature furnace. The furnace was programmed to gradually heat the samples up to 1000 °C, where they were held for 30 minutes to allow complete melting of the constituents. During this melting process, the mixture was manually shaken every 10 minutes to enhance uniformity. Following melting, the molten glass was rapidly quenched by pouring it onto a preheated brass mold to form glass specimens. The quenched samples were immediately transferred to a secondary annealing furnace set at 300 °C, where they were held for 2.5 hours to relieve internal stresses. This step annealing approach helped achieve a stable glass network and minimize residual stress. After annealing, the samples were allowed to cool slowly inside the furnace over a period of 24 hours until room temperature was reached, ensuring structural stability and preventing cracking. The complete glass preparation process is illustrated in Figure 1.

After annealing, the glass samples were cut into suitable sizes and polished using a series of silicon carbide (SiC) abrasive papers with progressively finer grits (from 400 to 1200) to obtain smooth surfaces for optical and structural analysis. For FTIR, XRD, and DSC/TGA powder-based characterizations, a portion of each glass sample was ground into fine powder using an agate mortar and pestle until a uniform particle size was achieved. The powdered samples were then stored in airtight containers to prevent moisture absorption prior to analysis. Figure 2 shows the prepared borate-based bioactive glass samples before and after polishing process. Visual clarity reflects the influence of CaO content on glass formation and structural integrity.

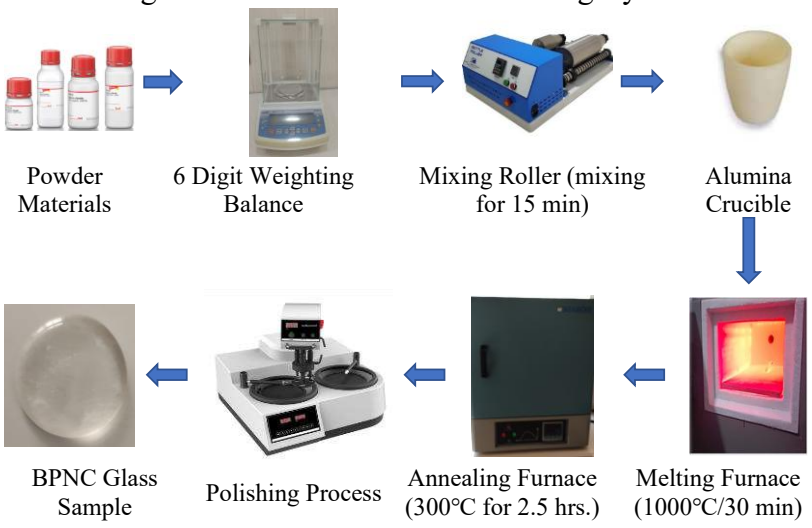

Figure 1: The experimental setups for the glass preparation process.

Table 1. Chemical composition of the prepared glasses.

Sample code	Mol % of oxides present in the sample			
	B_2O_3	P_2O_5	NaO	CaO
BPNC0	65	15	20	0
BPNC1	62.5	15	20	2.5
BPNC2	60	15	20	5
BPNC3	57.5	15	20	7.5
BPNC4	55	15	20	10
BPNC5	50	15	20	15

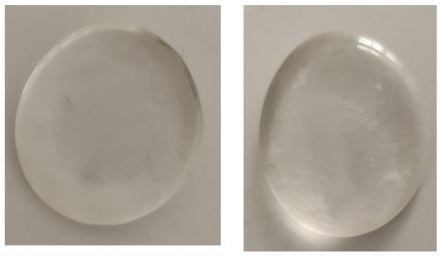

Before Polishing After Polishing

Figure 2: An image of Borate-based bioactive glass sample before and after polishing process.

The physical characterization of the prepared bioactive glass samples began with the measurement of density using Archimedes' principle. Each glass sample was weighed in air and then in distilled water as the immersion medium to determine its bulk density. This method provides an accurate evaluation of density based on the displacement of liquid and is widely used for glass materials. The density values were analyzed to assess the influence of CaO substitution on the glass network structure. As CaO content increased, variations in density were observed, which are indicative of changes in the packing density and connectivity of the glass network. These measurements are essential for understanding the structural compactness and potential mechanical behavior of the bioactive glasses. The density of the prepared glass samples was measured using Archimedes' principle, applying the following equation (1) [14] :

$$\rho = \rho_w\left(\frac{W_A}{W_A - W_W}\right) \qquad (1)$$

Where $\rho$the density of the glass sample is, ρ_w is the density of distilled water (used as the immersion fluid), W_A is the weight of the sample in air, and W_W is the weight of the sample when submerged in water. A high-precision six-digit electronic balance (Radwag AS 220.R1) was used to ensure accurate weight measurements. The measured density values are directly related to the structural network of the glass. Changes in density reflect alterations in the packing and connectivity of the glass structure caused by compositional modifications. To further explore these structural changes, the molar volume (V_M) of each sample was calculated using the following equation (2) [15] .

$$V_M = \frac{M}{\rho} \qquad (2)$$

Where M is the molecular weight of the glass composition.
Variations in molar volume with composition provide insights into the effect of oxide substitution on the openness or compactness of the glass network.

A Philips PW1730 diffractometer, which uses Cu kα radiation (wavelength = 1.5406 Å) as an X-ray source, was used to record the X-ray diffraction analysis (XRD). With a step size (2θ) 0.05° and a scan step time (1s), the scan area is 2θ = 10º–80º at 40 kV and 30 mA. Fourier Transform Infrared Spectroscopy (FTIR) was used to analyze the structural units and bonding characteristics of the prepared bioactive glass samples. The measurements were conducted using a (SHIMDZU

IRAffinity-1), operating in the spectral range of 400–4000 cm^{-1}. Finely ground glass powders were mixed with potassium bromide (KBr) and pressed into pellets to enhance spectral clarity. The FTIR spectra provided information on the presence of borate (BO_3 and BO_4), phosphate, and carbonate groups, and allowed investigation of structural changes related to varying CaO content in the glass network. UV-Vis-NIR spectrophotometer (Jasco770) was used at room temperature to calculate the absorption between the scanning wavelength range (200–900 nm), data interval (1 nm) UV-Vis-NIR bandwidth (5 nm) and NIR bandwidth (20 nm), The visible to near-infrared (Vis-NIR) spectrum, which spans from 330 nm to 1100 nm or beyond, is covered by tungsten-halogen lamps. Thermal behavior of the glass samples was investigated using simultaneous Differential Scanning Calorimetry–Thermogravimetric Analysis (DSC/TGA) employing an SDT Q600 thermal analyzer (TA Instruments, USA; software version V20.9 Build 20). The measurements were carried out under a nitrogen atmosphere at a controlled heating rate, allowing simultaneous evaluation of glass transition behavior, thermal stability, and mass loss characteristics.

3. Results and Discussion

3.1 Structural Characterizations

3.1.1 X-Ray Diffraction Analysis

The X-Ray Diffraction (XRD) patterns for all samples (BPNC0 to BPNC5) as shown in Figure 3 display broad humps centered around 20-35° 2θ, without any sharp crystalline peaks. This characteristic broad halo is a hallmark of amorphous (non-crystalline) glassy structures, indicating that all the prepared compositions retained a disordered network structure after melting and quenching. As the CaO content increases from BPNC1 to BPNC5, the intensity and shape of the halo slightly change, suggesting subtle rearrangements in the glass network. However, no distinct crystalline phases are observed, confirming that the incorporation of CaO up to 15 mol% does not induce crystallization under the given synthesis conditions. However, in the BPNC0 sample (with 0 mol% CaO), a weak crystalline peak is observed around ~27° 2θ. This suggests the presence of a minor crystalline phase in the base glass, possibly due to incomplete glass formation or localized phase separation. As CaO is introduced (BPNC1), this peak becomes less intense, indicating a reduction in crystallinity. In samples with higher CaO content (BPNC2-BPNC5), the peak disappears completely, confirming that the addition of CaO helps to stabilize the glass network and suppress crystallization. This transition supports the role of CaO as a network modifier that disrupts ordered regions and promotes amorphization. The absence of sharp diffraction peaks in BPNC1-BPNC5 confirms their fully amorphous nature, which is ideal for bioactive applications, as it typically enhances dissolution rates and bioactivity due to higher surface reactivity.

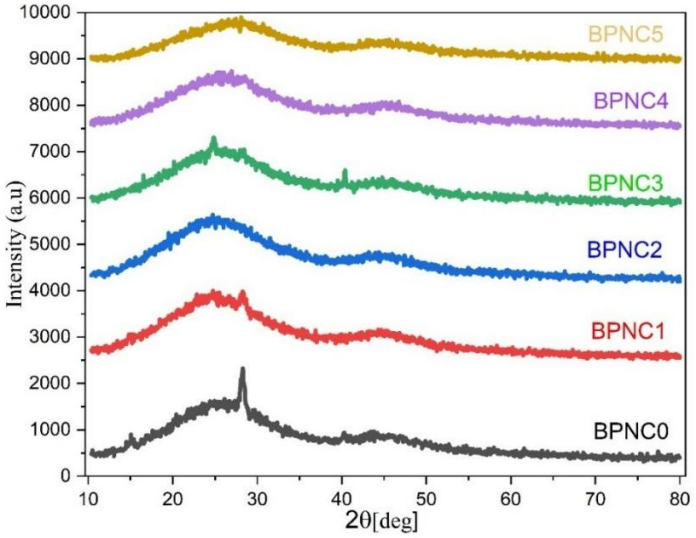

Figure 3: XRD patterns of bioactive glass samples with compositions (65-x) B_2O_3 + 15P_2O_5 + 20Na_2O + xCaO (mol%), where x = 0 to 15.

3.1.2 Fourier transform infrared Analysis

Fourier Transform Infrared (FTIR) spectroscopy is a powerful analytical technique that plays a crucial role in studying the structural characteristics and functional groups within glass materials. This method allows researchers to obtain into the molecular vibrations and interactions occurring within the glass matrix. The FTIR full spectra is presented in Figure 4 and for giving more clearly detailed information about the spectra, the spectra separated into three regions (a, b, c) offering visual confirmation of the modifications discussed. The systematic analysis of these FTIR spectra detailed in Table 2, illustrates the distinct bond positions and their corresponding assignments, providing a comprehensive understanding of the glass's structural dynamics. In the BPNC0 sample, several critical vibrational modes are identified. A notable feature is the bending vibration of HOH, detected in the range of 1465-1471 cm^{-1}, indicative of water or hydroxyl groups contributing to the glass network [16]. Additionally, the presence of B-O-B boroxyl linkages is observed between 500 and 650 cm^{-1}, providing insights into the connectivity of borate structures essential for the glass's stability and mechanical properties. The signature peak of BO_3, observed at 1270 cm^{-1}, suggests the presence of planar trigonal boron coordination, highlighting a conversion of some BO_4 units into BO_3 configurations. This change underscores the glass composition's adaptability as modifications are applied [17]. Furthermore, the P-O-P stretching vibration appears prominently at 1050 cm^{-1}, reflecting the structural integrity of phosphate links within the glass matrix. As calcium oxide (CaO) is introduced starting at a 2.5% concentration its influence on the vibrational characteristics becomes evident. A significant transition is noted with the formation of O-P-O phosphoryl bridges in the range of 560-604 cm^{-1}, specifically at 964 and 1045 cm^{-1}. This suggests the bridging of oxygen species and retention of connectivity in the phosphate network [18].

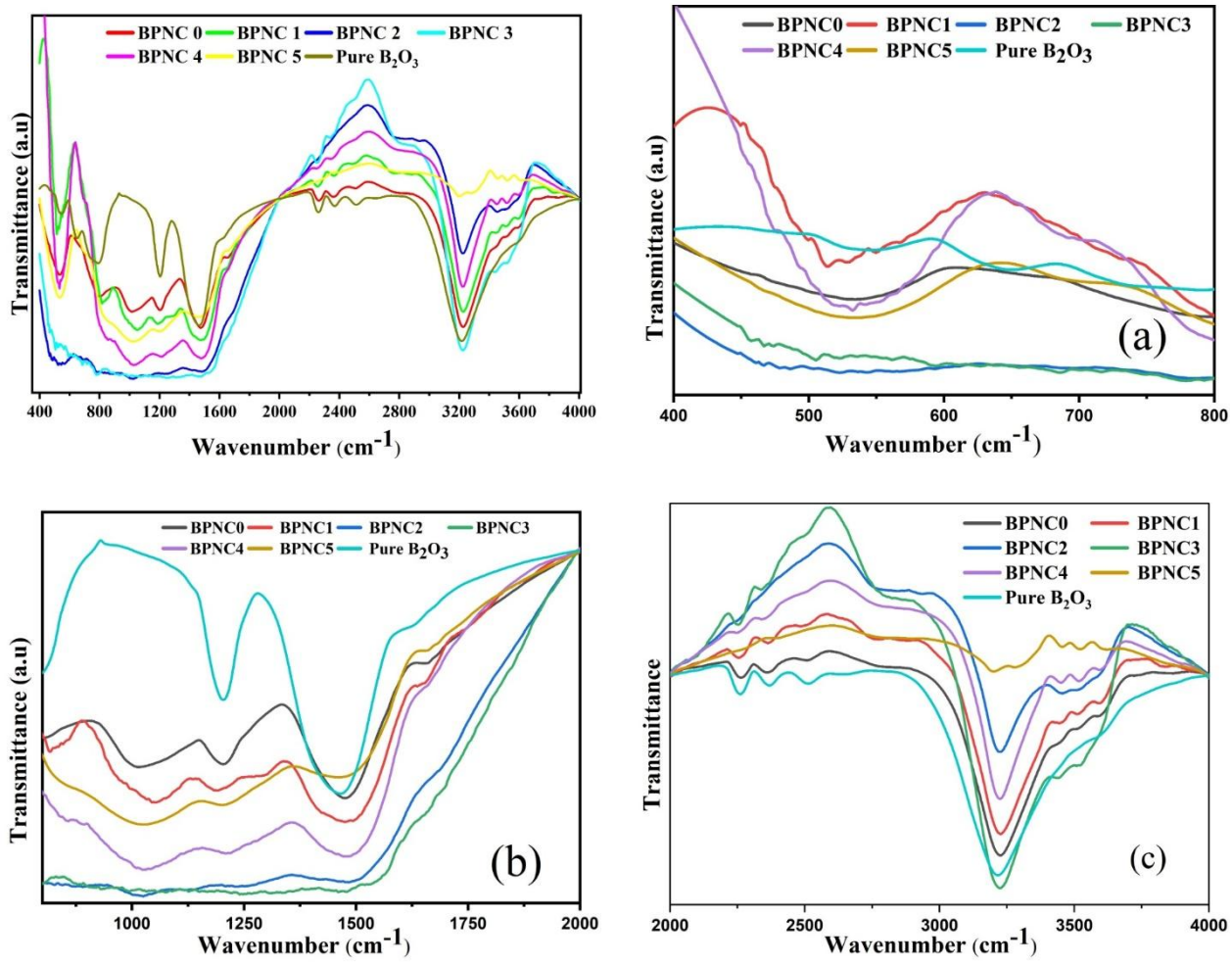

Figure 4(a,b,c): FTIR spectra of BPNC glass in the range of 400-4000 cm^{-1}
((4a) 400-800 cm^{-1}, (4b) 800-2000 cm^{-1}, (4c) 2000-4000 cm^{-1})

The introduction of CaO also facilitates the emergence of non-bridging oxygens (NBOs), as suggested by the P-O bond detected around 500 cm^{-1}. experiences a diminishing intensity, ranging from 3520 to 3454 cm^{-1}, hinting at hydrogen bonding interactions with the newly formed NBOs. Upon reaching a 5% CaO concentration, the formation of M-OH metallic bonds between 400 and 1600 cm^{-1} becomes evident. This modification aids in enhancing electrical conductivity and ionic interactions among metal ions, while concurrently implying a disruption of existing covalent networks. emergence of the POP bond at 680 cm^{-1} for BPNC3 sample, signaling a restoration of the phosphate network [19]. This concentration also produces a complex of P-O bonds across multiple wavelengths (560, 604, 1050, and 500 cm^{-1}), signifying the persistent influence of modifiers on the overall structure and connectivity of the glass. The OH bond remains detectable at 3485 cm^{-1}. Progressing to a 10% CaO level, the changes in the FTIR spectrum reflect a further evolution of the glass structure. The BOB linkage reappears at 1259 cm^{-1}, suggesting reformation of borate connectivity. Meanwhile, the PO peak at 1050 cm^{-1} indicates a greater presence of non-bridging oxygen species, leading to a depolymerized phosphate structure. The M-OH bond shifts to 3444 cm^{-1}, indicating a balance is established among both phosphate and borate networks, likely due to the introduction of Ca^{2+} ions. At 15% CaO, the effects on the vibrational landscape become even more pronounced. Notably, the HOH bending occurs between 1629 and 1653 cm^{-1}, indicative of physically absorbed water or hydroxyl interacting with NBOs [20]. The hydroxyl bond at 3441 cm^{-1} indicates continued structural evolution. Throughout all sample modifications, it is evident that the introduction of CaO consistently promotes the formation of BO_3 at 1270 cm^{-1}, reflecting a fundamental alteration in the glass's borate structure [21].

Table (2): FTIR band positions and vibrational assignments for BPNC glass system.

Assignment	Band Position (cm^{-1})					
	BPNC0	BPNC1	BPNC2	BPNC3	BPNC4	BPNC5
O-P-O Phosphoryl Bridge	-----	560-600 964-1045	-----	-----	-----	-----
H-O-H Bending Vibration	1465-1471	-----	-----	-----	-----	1629 1653
B-O-B Boroxyl Linkage (BO_3)*	500 – 650	(1270)*	(1270)*	(1270)*	1259 (1338)*	1033 (1270)*
P-O-P Stretching Vibration	1050	-----	-----	680	-----	600 ,700, 981 and 925
P- O (PO_2)*	-----	500	-----	560- 604- 1050- 500	1050	549 1050 (1386)* (1420)*
M − OH Metallic Bond	-----	-----	400 to 1600	-----	491 – 561	-----
OH Hydroxide Bond Group	3215 – 3446	3520 3454	3487	3485	3444	3441

3.2. Physical properties

3.2.1 Density (ρ) and molar volume (V_M)

Density and molar volume are key parameters in understanding the structural behavior of glasses. Table 3 presents the glass compositions along with their corresponding molar mass, density, molar volume, and color. The base glass without CaO exhibits a density of 2.163 g/cm^3. With the

addition of 2.5 mol% CaO, the density increases to 2.444 g/cm^3, likely due to CaO filling voids within the glass network. However, when CaO content is increased to 5 mol%, the density decreases to 2.337 g/cm^3. This reduction may be attributed to the formation of non-bridging oxygen (NBO) bonds between boron and calcium, which can disrupt the glass network. As the CaO content increases to 7.5 and 10 mol%, the density rises again to 2.532 g/cm^3, possibly due to further structural rearrangement and more efficient packing within the network. At 15 mol% CaO, the density slightly decreases to 2.499 g/cm^3, potentially due to the generation of additional NBOs that reduce the packing efficiency. Overall, density variations reflect the structural role of CaO as a network modifier. A decrease in density is generally associated with the formation of NBOs through the breaking of B–O bonds, while an increase indicates the integration of Ca^{2+} ions into the network, enhancing packing and reducing interatomic distances. Moreover, the presence of heavier CaO atoms contributes to increased density by drawing atoms closer together [23].

Figure 5 illustrates the variation of density and molar volume with increasing CaO content in the synthesized glass samples. An overall inverse relationship is evident: as density increases, molar volume tends to decrease, reflecting tighter atomic packing and reduced interstitial spaces in the glass network. The base glass without CaO exhibits the lowest density (~2.16 g·cm^{-3}) and the highest molar volume (~46.5 cm^3·mol^{-1}), indicating a loosely packed structure. Upon adding 2.5 mol% CaO, the density increases while molar volume decreases sharply, suggesting that Ca^{2+} ions act as network modifiers, occupying interstitial voids and enhancing network compaction. This densification trend continues, with minor fluctuations, up to 10 mol% CaO, after which the structure appears to stabilize. The observed changes in molar volume and density have direct implications for bioactivity. A denser and more compact glass structure typically associated with lower molar volume can influence the rate of ion exchange with physiological fluids. In particular, Ca^{2+} ions play a crucial role in forming (HCA) layer on the glass surface, which is essential for bonding with bone tissue [24]. However, excessive densification can reduce the rate of ion release, potentially limiting bioactivity, while too loose a structure may compromise mechanical integrity. Therefore, controlling the molar volume and density through optimized CaO content is vital for balancing structural strength and bioactivity. Glasses with intermediate CaO content (e.g., 5–10 mol%) appear to offer a favorable balance, supporting both controlled degradation and effective bioactive response[25, 26].

Table 3 Presents the values for Average molar mass (M) (g.mol^{-1}), Density ($\rho \pm 0.01338$) (g/cm^3), molar volume ($V_M \pm 0.26853$) (cm^3. mol^{-1}), and Color.

Code	M	ρ	V_M	Color
BPNC0	100.232	2.163	46.3395	bright colorless
BPNC1	99.8939	2.444	40.8731	bright colorless
BPNC2	99.5554	2.337	42.5996	bright colorless
BPNC3	99.2169	2.416	41.0665	bright colorless
BPNC4	98.8783	2.532	39.0514	bright colorless
BPNC5	98.2013	2.499	39.2962	bright colorless

As shown in Figure 6, all glass samples display a clear, colorless, and transparent appearance across the CaO compositional range, indicating good homogeneity and amorphous structure. The base glass (BPNC0) without CaO maintains high clarity, and similar optical quality is preserved up to 10 mol% CaO (BPNC1-BPNC4). However, a slight reduction in transparency is observed in BPNC5 (15 mol% CaO), which may be attributed to increased non-bridging oxygen formation or phase separation during cooling. This visual consistency is crucial for bioactive glass applications, where transparency can be an indirect indicator of uniformity and purity essential for predictable ion release and biological response[25]. Moreover, the CaO content plays a key role in modulating bioactivity: moderate additions enhance the formation of calcium phosphate layers upon implantation, while

excessive CaO may disrupt network connectivity and reduce bioactive performance [26] . Thus, the visual and structural properties together suggest that compositions up to 10 mol% CaO offer optimal balance for bioactive glass use.

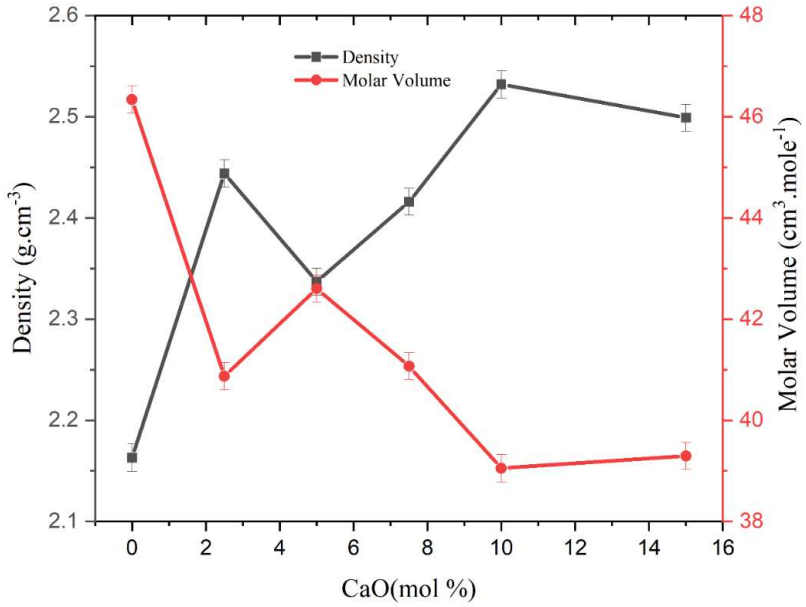

Figure 5: Variation of density and molar volume of the glass samples as a function of CaO content.

Figure 6: Borate-based bioactive glass samples with compositions (65–x) B_2O_3 + 15P_2O_5 + 20Na_2O + xCaO (mol%), where x = 0 to 15. Samples are labeled BPN and BPNC1–BPNC5 based on CaO content.

3.2.2 Inter-nuclear distance, concentration, field strength and polaron radius.

The density and molecular volume curve of glasses can be explained by the internal spatial organization of the materials. The molar volume of Boron (V_m^B) and the average boron-boron separation $\langle d_{B-B} \rangle$ have been calculated to confirm the compaction of glasses brought on by Calcium oxide. This shows that the following equations (3) through (4) were used to determine the volume of the structure containing one mole of boron, accordingly.[27, 28]

$$V_m^B = \frac{V_m}{2(1 - X_B)} \qquad (3)$$

$$\langle d_{B-B} \rangle = \left(\frac{V_m^B}{N_A}\right)^{\frac{1}{3}} \qquad (4)$$

Where are $V_m^B . X_B \; and \; N_A$ are molar volume of glass, mole fraction of B_2O_3 and Avogadro's number. The anticipated ion concentrations in these glasses can be found using the formula below.

$$N = \frac{X_{Ca} * N_A * \rho}{M} \qquad (5)$$

Where $X_{Ca} . \rho \; and \; M$ represent the molar fraction of Ca, density, and molecular weight of the glass, respectively. Based on the ion concentrations, another important physical parameter can be computed,

such as the inter-nuclear distance (R_i) of CaO , the polaron radius (R_p) of CaO , and field strength (F) were calculated using the following equations (6)–(8) respectively [29]:

$$R_i = \left(\frac{1}{N}\right)^{\frac{1}{3}} \qquad (6)$$

$$R_P = \frac{1}{2}\left(\frac{\pi}{6N}\right)^{\frac{1}{3}} \qquad (7)$$

$$F = \frac{Z}{R_P^2} \qquad (8)$$

Where Z is the oxidation state of Ca ions.

The average coordination number (m) and number of bonds per unit volume (n_b) were calculated from formula (9) and formula (10), respectively[30].

$$m = \sum_i X_i N_i \qquad (9)$$

$$n_b = \frac{N_A}{V_m} m \qquad (10)$$

Where X_i and N_i represent molar fraction and coordination number of the cations.

Table 4 : The physical parameters molar volume of Boron (V_m^B), average boron-boron separation $< d_{B-B} >$, Ion concentrations of CaO (N_{Ca}) , inter-nuclear distance ($R_i \pm 0.04133$) of CaO, the polaron radius ($R_P \pm 0.04103$) of CaO , field strength (F), average coordination number (m), number of bonds per unit volume (n_b), Oxygen molar volume ($OMV \pm 0.05905$), oxygen packing density ($OPD \pm 0.25838$) and number of oxygen atoms in the glass system (O_n) of the glass samples for various CaO concentrations.

Parameters	Sample code					
	BPNC 0	BPNC1	BPNC2	BPNC3	BPNC4	BPNC5
$V_m^B(cm^3 \cdot mol^{-1})$	66.21	54.51	53.25	48.31	43.39	39.31
$< d_{B-B} > (\times 10^{-8} cm)$	4.79	4.49	4.45	4.31	4.16	4.02
$N_P(\times 10^{23} ion\ cm^3)$	0	0.3682	0.7065	1.099	1.541	2.297
$R_i(A^\circ)$	0	3.005	2.418	2.087	1.865	1.632
$R_p(A^\circ)$	0	1.2	0.97	0.84	0.75	0.66
$F(\times 10^{16} \cdot cm^{-2})$	0	1.363	2.105	2.827	3.541	4.621
m	3.35	3.325	3.3	3.275	3.25	3.2
$n_b(\times 10^{22} cm^{-3})$	4.352	4.897	4.663	4.800	5.010	4.902
OPD	62.58	69.73	65.73	66.96	69.14	66.17
$OMV(cm^3 \cdot mol^{-1})$	15.98	14.34	15.21	14.93	14.46	15.11
O_n	2.9	2.85	2.8	2.75	2.7	2.6

The interactions between charge carriers and lattice ion vibrations in extremely polar or ionic solid materials produce polarons, which are miniature particles [31, 32]. Polarons have an impact on a number of processes, such as optical absorption, electron transport, and chemical reactivity [33].

The field strength, polaron radius, inter-nuclear distance (R_i) of CaO, average boron-boron separation $< d_{B-B} >$, molar volume of boron (V_m^B), number of bonds per unit volume, and average coordination number are presented in Table (3). Strong network former CaO brings PO_4 tetrahedra into the framework. Rivals B_2O_3 in network building, the competition between the B-O-B and B-O-Ca bonds modifies the structure that influences the separation of B as the CaO grows.

Alterations in P_2O_5 and Na_2O, B-O-Ca connections, and the disintegration of the B_2O_3 network define the alterations. Whereas the cation concentration of CaO increases from 0.3682×10^{23}

to 2.297 × 10^{23} ions per cm^3 as CaO molar fraction increases. The polaron radius and inter-nuclear distance are decreased the polaron radius decrease from 1.2Å to 0.66 Å and inter-nuclear distance decrease from 3.005Å to 1.632Å with increasing CaO content as both parameters depended on the concentration and disordering distribution in atoms that cause to this state and that is amorphous the changing oxygen bridge atoms to non-oxygen bridge atoms.
The linear atomic ionic displacement field of a polaron is called its polaron radius. The polaron is referred to as a small polaron when its radius is on the order of the lattice constant. A big polaron occurs when the radius is significantly greater than the material's lattice constant. Since the numbers fall below the lattice constants of the various oxides in the glass, they imply that the polaron is a tiny polaron. The increase in glass polarizability and compactness could be linked to the decrease in the polaron radius. The electrical conductivity of glass may gradually rise as a result [32, 34].
The field strength trend and the polaron radius trend are in opposition to one another.
The field strength increases from 1.363× 10^{16} cm^{-2} to 4.621× 10^{16} cm^{-2}, this may be attributed to the increase in Ca–O bond strength and reduction in Ca–O bond length. The variation of the polaron radius and the internuclear distance with CaO content is depicted in figure (7), demonstrating a clear dependence of these parameters on the CaO concentration. As the CaO content increases, noticeable changes in the polaron radius are observed, suggesting alterations in charge carrier localization within the glass/network structure. Simultaneously, the internuclear distance exhibits corresponding variations, reflecting structural rearrangements and modifications in the bonding environment caused by the incorporation of CaO [34].

In figure (7), both R_p and R_i initially increased sharply with the addition of 2.5 mol% CaO, reaching peak values of ~1.2 Å and ~3.005, respectively. This suggests that the initial Ca^{2+} incorporation into the glass network expands the electron cloud and increases the average spacing between ions, likely due to structural loosening and the creation of non-bridging oxygen (NBO) sites. As CaO content increases beyond 2.5 mol%, a gradual decline in both parameters is observed. The polaron radius decreases more significantly than the internuclear distance, indicating enhanced structural compactness and reduced delocalization of charge carriers. This can be attributed to the role of Ca^{2+} as a network modifier, which at higher concentrations helps stabilize the structure and reduce the mobility of electrons or holes in the glass matrix. From a physical standpoint, the decreasing trend in R_p and R_i at higher CaO content implies a more tightly packed structure with limited electronic delocalization, which may impact the electrical, optical, and bioactive behaviors of the glass. Notably, a reduced R_p may hinder polaron hopping and reduce conductivity, but it can also enhance mechanical strength and chemical durability, both of which are advantageous for bioactive applications.

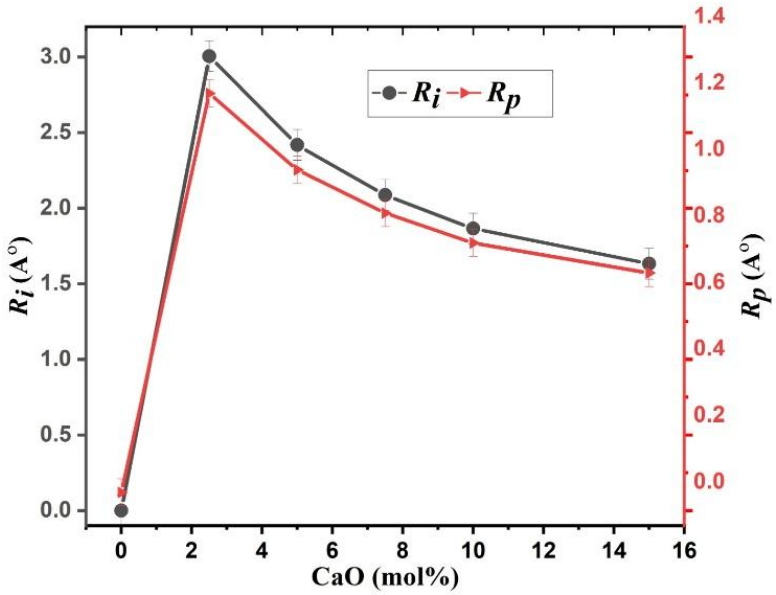

Figure 7: Variation of polaron radius (R_P) and internuclear distance (R_i) as a function of CaO content in the glass system.

3.2.3 Oxygen molar volume (OMV) and oxygen packing density (OPD)

The oxygen molar volume (OMV) was calculated based on molar volume:

$$OMV = \frac{V_m}{\sum_i n_i x_i} \qquad (11)$$

Where n_i and x_i in equation (11) represent the fraction of the oxygen atoms in each element and the molar fraction of the oxides of the fabricated glasses, respectively.
To gain a better understanding, the oxygen packing density (OPD) has been calculated using the formula based on the density and molar volume values. [35]

$$OPD = 1000 * \frac{O_n}{V_m} \qquad (12)$$

Where O_n represents the number of oxygen atoms in the glass system and it can be calculated as follows:

$$O_n = X_B * N_{OB} + X_P * N_{OP} + X_{Na} * N_{ONa} + X_{Ca} * N_{OCa} \qquad (13)$$

where X_B, X_P, X_{Na} , $and\ X_{Ca}$, N_{OB}, N_{OP} , $N_{ONa} and\ N_{OCa}$ represent the molar fraction of B_2O_3, P_2O_5 ,Na_2O and CaO number of oxygen's in B_2O_3, P_2O_5 ,Na_2O and CaO respectively.
The outcomes of this method demonstrate the opposite relationship. The OMV rises and the OPD falls, as indicated in Table 4 and Figure 8. The development of additional bridging oxygen's, which eventually aid in the creation of a compact glass structure, makes this behavior apparent [36]. The total number of oxygen's decreased from 2.9 to 2.6 due to a decrease in B_2O_3 content. The evolution of NBO atoms and the extension of the structure are indicated by the variations in OPD with CaO amount. The expansion of the glass structure caused by the increase in the CaO component is in good agreement with the molar volume measurements, the prepared glasses' data revealed the opposite pattern. The strong OPD increases from 62.58 to 66.17, while OMV decreases from 15.98 to 15.11 when the concentration of CaO increases. The increase in OPD together with the decrease in OMV indicates a more compact and tightly packed glass network, suggesting an enhancement rather than a weakening of the glass structure upon CaO addition.

Figure 8 illustrates the effect of CaO content on the (OMV) and (OPD) of the glass system. OMV refers to the average volume occupied per mole of oxygen atoms in the glass matrix, while OPD measures how densely oxygen atoms are packed in the structure. At 0 mol% CaO, OMV is highest (15.98 cm^3/mol), indicating a loose packing of oxygen atoms. The corresponding OPD is relatively low (~62.5), suggesting a more open network with lower atomic density. With the addition of 2.5 mol% CaO, a sharp decrease in OMV and a significant increase in OPD are observed. This suggests that Ca^{2+} ions fill voids in the glass structure and promote tighter packing of oxygen atoms, enhancing the structural compactness [36].

However, further increases in CaO (from 5 to 10 mol%) cause fluctuations in both OMV and OPD. These variations reflect competing effects: while CaO addition tends to compact the network, it also introduces non-bridging oxygen (NBO), which may expand local structures and disrupt uniform oxygen packing. At 10 mol% CaO, OPD reaches a secondary peak, suggesting a more optimized oxygen arrangement, while OMV reaches a local minimum (14.46 cm^3/mol), consistent with increased network compactness. Beyond 10 mol%, OMV increases slightly while OPD decreases, indicating that excessive CaO may begin to disrupt the glass network and reduce packing efficiency, likely due to the formation of more NBOs. These findings are significant for bioactive glasses, where the oxygen structure plays a key role in ion release and surface reactivity. A well-packed oxygen network (high OPD, low OMV) generally enhances mechanical stability and controlled bioactivity, while looser structures may facilitate faster degradation but lower mechanical integrity [37].

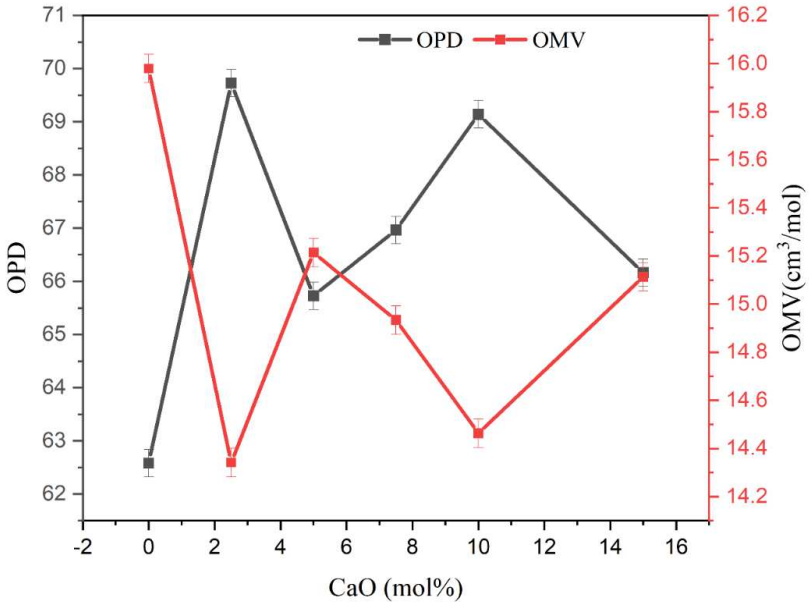

Figure 8: Variation of oxygen packing density (OPD) and oxygen molar volume (OMV) with CaO content in sodium borophosphate glasses

3.3 Optical Properties

3.3.1 Absorption Spectra

Figure 9 shows the UV-Vis-NIR absorption spectra of glass samples in the wavelength interval of 200 to 900 nm. The absorbance spectra of the BPNC glass samples exhibit a strong absorption in the UV region (200–350 nm), which is typical for phosphate and borate-based glasses due to electronic transitions related to (NBO) and metal-oxygen bonds. As the CaO content increases, a general trend of increasing absorbance is observed, especially in the BPNC5 sample, which shows a significantly higher absorbance intensity across the spectrum. This increase may be attributed to a higher concentration of NBOs formed due to CaO acting as a network modifier, disrupting the glass network and creating more localized electronic states that absorb in the UV region. Additionally, the blue shift of the absorption edge in lower CaO content samples (e.g., BPNC2) suggests a widening of the optical band gap, while the red shift and increased absorbance in BPNC5 indicates band gap narrowing. These changes in optical properties are crucial for tuning bioactive glass materials for medical applications such as photothermal therapy, UV shielding, or enhanced photocatalytic response [38].

The absorption coefficient (α), which quantifies how much light is absorbed per unit thickness of the material, can be calculated using the relation:

$$\alpha = 2.303 \times 10^{-3} A\, L^{-1} \qquad (14)$$

Where A is absorbance and L the sample thickness in cm. Direct and indirect energy bandgap values were determined using the absorption spectra method developed by Davis and Mott [39].

$$\alpha\hbar\omega = B(\hbar\omega - E_{Opt})^{n} \qquad (15)$$

$$(\alpha\hbar\omega)^{1/n} = B(\hbar\omega - E_{Opt}) \qquad (16)$$

Where α,$\hbar\omega$, and B are the absorption coefficients, photon energy, and electronic transition constants, respectively as shown in Figure 9. The type of electronic transition determines the exponent n in Tauc's equation: (n = 1/2) for allowed direct transitions, (n = 2) for allowed indirect transitions, and (n = 3/2) for forbidden transitions. This equation describes how much light of a specific energy is absorbed by a material of a given thickness. To estimate the optical bandgap energy, Tauc plots are

used by graphing $(\alpha\hbar\omega)^{1/n}$ versus photon energy ($\hbar\omega$). The linear portion of the plot is extrapolated to intersect the energy axis at $(\alpha\hbar\omega)^{1/n} = 0$, indicating the optical bandgap (Davis and Mott, 1970). The bandgap energy values reflect structural changes in the glass. As shown in Table 5 and Figures 10 and 11, the direct and indirect bandgap energies of the BPNC samples tend to decrease with increasing CaO content, although the trend is somewhat irregular. These variations can be attributed to changes in the glass network structure and bonding as more CaO is incorporated

Figure 12 presents the variation of both direct and indirect optical bandgap energies of BPNC glass samples as a function of CaO concentration (mol%). The black curve represents the indirect bandgap (E_{ind}), while the red curve corresponds to the direct bandgap (E_{dir}). As the CaO content increases, the indirect bandgap shows a fluctuating trend, initially increasing up to 5 mol% CaO and then decreasing slightly before rising again at 15 mol%. This behavior reflects structural rearrangements within the glass network caused by CaO, which modifies the bonding environment and the degree of disorder. In contrast, the direct bandgap remains nearly constant from 0 to 10 mol% CaO as shown in Figure 12, with minor variations, but shows a significant drop at 15 mol%, indicating a possible structural phase change or the formation of non-bridging oxygens that affect the electronic transitions. As the cation concentration increases, it is believed that (BO) form bonds with phosphorus, leading to a gradual disruption of the glass network. This breakdown results in an increase in (NBO) content, as reflected by the observed decrease in bandgap energy. The shift in the absorption edge further indicates changes in the oxygen bonding environment within the glass matrix. The difference in the trends of the indirect optical band gap (E_{ind}) and direct optical band gap (E_{dir}) arises due to the distinct nature of electronic transitions involved. E_{dir} corresponds to direct allowed transitions, while E_{ind} corresponds to indirect transitions that involve phonon participation. Therefore, their magnitudes and slight variations with composition can differ, even though the overall compositional trend is consistent [40].

Urbach energy (E_U) which aids in the calculation of variations in glass material defects, is the range of certain energy levels related to light transitions between specific states in the valence band and broader ones in the conduction band. A logarithmic equation (17) and the slope of a straight line on a graph of $\ln(\alpha)$ vs $\hbar\omega$ are used to measure it. It is measured using the logarithmic equation (17) and the reciprocal of the slope at the linear part of a plot between $\ln(\alpha)$ vs. $\hbar\omega$ [41].

$$\ln(\alpha) = D + \frac{\hbar\omega}{E_U} \qquad (17)$$

Where D is constant and E_U is Urbach energy, it is equal to 1/slope

The relaxation of exaction-phonons or electron-phonons brought on by the growth of optical absorption is indicated by the steepness parameter (β). By using the equation, one may get the steepness factor based on the E_U [42] .

$$\beta = \frac{K_B T}{E_U} \qquad (18)$$

Where K_B Boltzmann constant and T room temperature in Kelvin unit.

The relationship between CaO concentration and the optical disorder in the glass matrix is illustrated in Figure 12 and Table 5 provides a comparative analysis between the prepared BPNC glass samples and previously reported glass systems. It includes key optical parameters such as cut-off wavelength, indirect and direct band gap energies, Urbach energy, and the steepness parameter. The comparison highlights how the optical properties of the synthesized glasses align with or differ from those in the literature, offering insights into the structural and electronic behavior of the developed glass system. Which presents the variation of Urbach energy and steepness parameter with CaO content. Urbach energy reflects the degree of structural disorder or defect states in the glass network, with higher values indicating greater disorder. Conversely, the steepness parameter is inversely related to Urbach energy and signifies the sharpness of the absorption edge; larger values imply a more ordered structure. As shown, Urbach energy exhibits a peak at 7.5 mol% CaO, suggesting that this composition introduces the highest degree of structural disorder [43]. Meanwhile, the steepness

parameter shows a corresponding dip, further confirming the presence of increased disorder at this concentration. At higher CaO levels (15 mol%), Urbach energy decreases while the steepness parameter increases sharply, indicating a recovery of structural order. As illustrate in Figure 13. These fluctuations demonstrate that the incorporation of CaO significantly affects the glass structure, influencing the degree of non-crystalline defects and optical edge sharpness [44]. The nonlinear variation of the indirect optical band gap (E_{ind}) shown in Figure 12 and Table 2 is mainly attributed to composition-induced structural changes in the glass network. Variation in glass composition modifies the bond strength, cation field strength, and concentration of non-bridging oxygens (NBOs), which introduces localized electronic states near the band edges and results in a non-linear dependence of E_{ind} on composition [45]. A clear correlation exists between E_{ind} and the physical properties of the glass series. The observed decrease in E_{ind} is associated with higher density and refractive index and lower molar volume, indicating increased electronic polarizability and network compactness. Enhanced polarizability increases orbital overlap, leading to band gap narrowing, whereas higher E_{ind} corresponds to a more polymerized and rigid glass network [46].

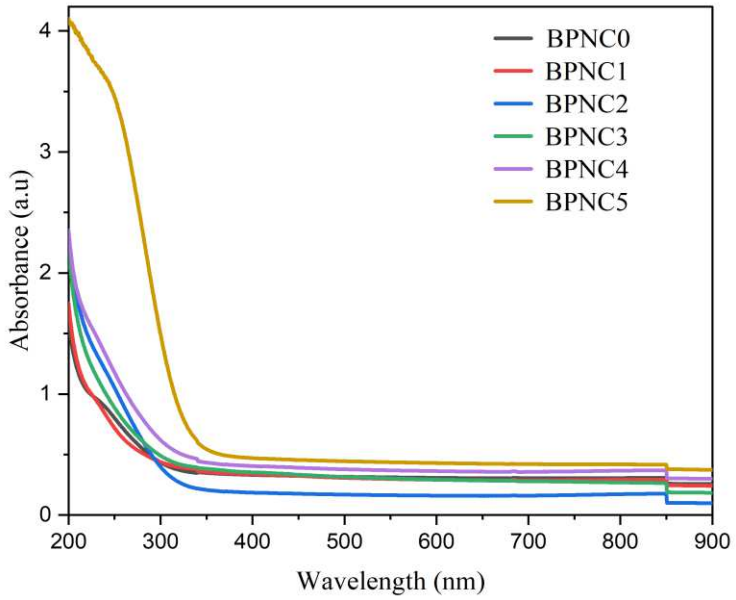

Figure 9: Absorption spectra for BPNC samples

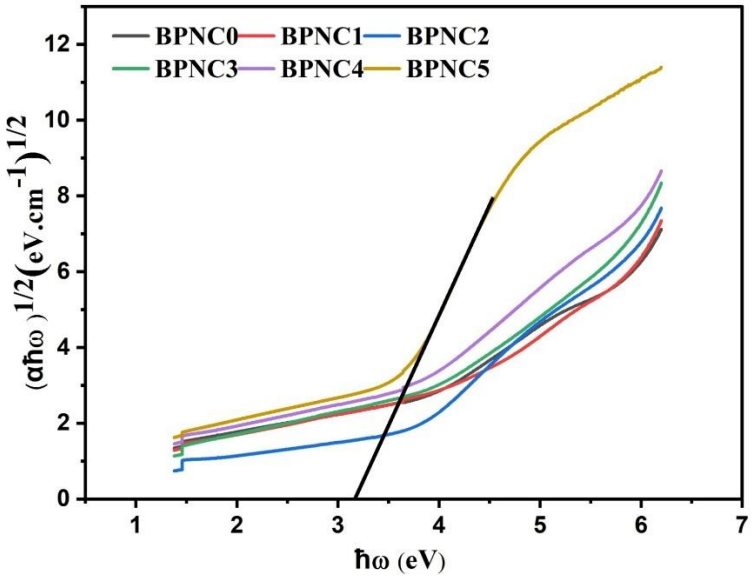

Figure 10: Tauc plots for direct band gap determination of BPNC samples with varying CaO content.

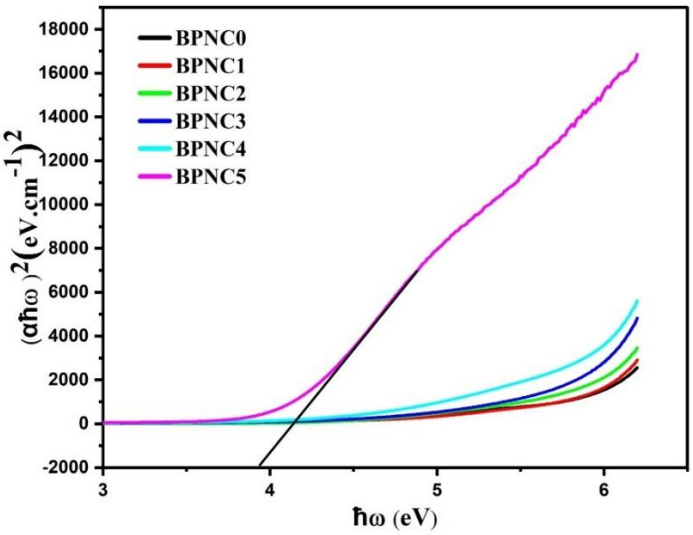

Figure 11: Tauc plots for indirect band gap determination of BPNC samples with varying CaO content.

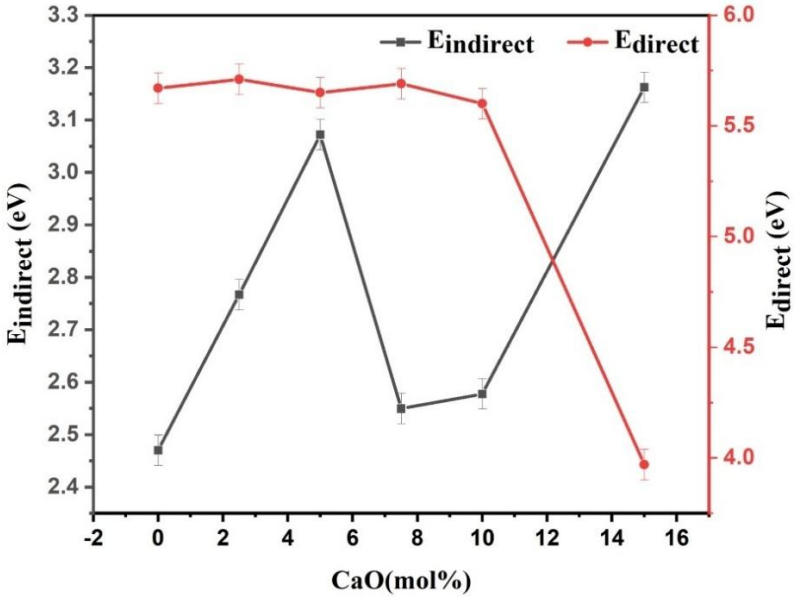

Figure 12: Variation of direct and indirect optical bandgap energies of BPNC glass samples as a function of CaO content.

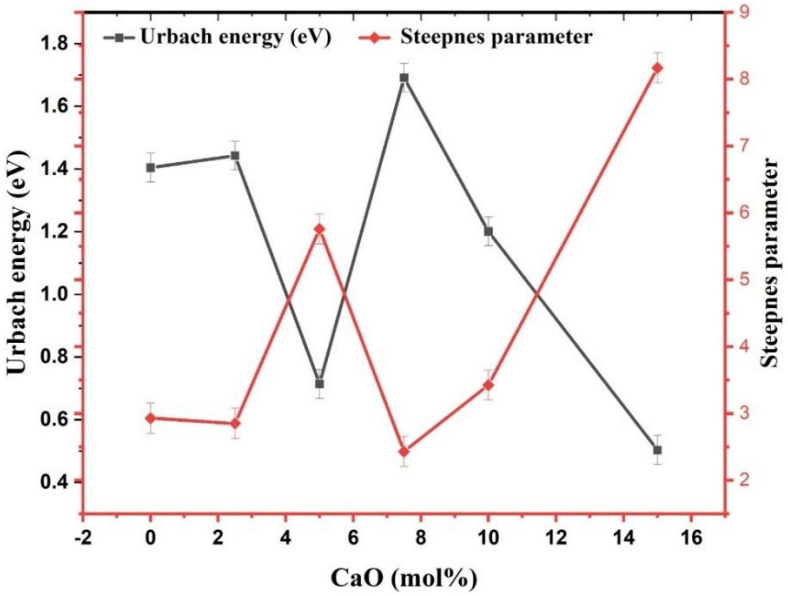

Figure 13: shows the variation of Urbach energy and steepness parameter with increasing CaO concentration in BPNC glass samples.

Table 5: summarizes the key optical parameters of BPNC glasses with varying CaO content, including cut-off wavelength (λ_{cut}) (nm), indirect energy bandgaps (E_{ind}± 0.029) and direct energy bandgaps (E_{dir}± 0.06926) (eV), Urbach energy (E_U± 0.04589) (eV) and steepness parameter (β± 0.22506).

Code	λ_{cut}(nm)	E_{ind}(eV)	E_{dir} (eV)	E_U (eV)	β (10^{-21})	References
BPNC0	341	2.47011	5.67	1.403	2.929	[47,48]
BPNC1	318	2.76717	5.71	1.442	2.850	[49]
BPNC2	325	3.07202	5.65	0.714	5.758	[50]
BPNC3	298	2.54966	5.69	1.691	2.431	[51]
BPNC4	342	2.57755	5.6	1.200	3.425	[52]
BPNC5	348	3.16232	3.97	0.503	8.169	[49,51]

3.3.2 Refractive index

Refractive index (n) is one of the intriguing properties of optical glass, varies with glass composition. The optical bandgap was used to compute direct and indirect refractive indices.

$$\frac{n^2-1}{n^2+2} = 1 - (\frac{E_{Opt}}{20})^{1/2} \qquad (19)$$

In equation (19), E_{Opt} and n represent the optical energy bandgap and the refractive index of the glass, respectively. The refractive index of glass is the result of the interaction between the electrons in the glass atoms and the incoming light. Consequently, a constant (called polarizability) specific to each material determines the degree of polarization or deformation of the orbitals. This polarization defines the light refraction, one well-known relationship for figuring out molar polarizability is the Lorentz-Lorentz equation[45]. For example, the total polarizability per unit mole of substance is known as molar refraction. The Lorenz equation can be used to calculate the molar refraction R_M of non-crystalline substances [46].

$$R_M = \frac{n^2-1}{n^2+2} V_M \qquad (20)$$

For isotropic substances such as cubic crystals, liquids, and glasses, Equation (20) provides the average molar refraction. The degree to which an electron in a material reacts to an electromagnetic field is known as polarizability. The molar refractive index (R_M) and Avogadro's number (N_A) were used to calculate the molar polarizability [53].

$$\alpha_e = \frac{3}{4\pi} \frac{V_M}{N_A} \qquad (21)$$

The composition of bioactive glass (65-x) B_2O_3 + 15 P_2O_5+ 20 Na_2O + x CaO, were x=0, 2.5, 5, 7.5, 10 and 15 of CaO, had its optical transmission (T_{opt}) and reflection loss (R_L) figured out using Eqs. (22) and (23) [54].

$$T_{opt} = \frac{2n}{n^2+1} \qquad (22)$$

$$R_L = (\frac{n-1}{n+1})^2 \qquad (23)$$

The parameters in Equations (20), (22), and (23) R_M, T_{opt} and R_L were calculated using the indirect refractive index. This is because the studied glasses exhibit an indirect band gap, as confirmed from the Tauc analysis. Using n_{ind} provides a more accurate estimation of these optical parameters since the electronic transitions in these glasses are predominantly phonon-assisted, which directly influences the optical response. Table 6 presents the results for different BPNC samples, including their direct and indirect refractive indices, molar refractivity, polarizability, optical transmittance, and reflection loss with CaO concentration. Figure 14 shows the variation in both indirect and direct refractive indices of the glass samples as a function of CaO concentration. The indirect refractive index starts at approximately 2.47 eV for the CaO free sample (BPNC0) then increases to 2.77 eV at 2.5 % CaO, indicating a disruption in the glass network due to the introduction of calcium ions. This

value increases to 3.07 eV at 5% CaO, suggesting partial network stabilization, before declining to its of 3.16 at 15% CaO, and at 7.5 % and10% CaO about 2.5 eV very near together the direct refractive index remains relatively stable between 5.6 eV and 5.71eV at 0 % to 10 % CaO, then sharply decrease to 3.97 at 15 % CaO shown in Figure 14, possibly due to increased formation of non-bridging oxygen [55]. The observed trends in refractive indices are consistent with structural changes and variations in optical density resulting from CaO incorporation into the borophosphate glass network. The interaction of incident light with the electrons in the glass atoms results in the refractive index of glass. Calcium oxide concentration affects the refractive index; it is observed that when concentration increases, the refractive index values alter. The addition of CaO modifies the glass network by increasing the number of non-bridging oxygens (NBOs), leading to a depolymerization of the glass structure. The glass structure is changed by the NBO, causing the molecules to be packed closer together. Because the refractive index and glass density are strongly correlated, glasses with higher densities will have higher refractive indices. The remarkable low of NBOs is the reason for the notable low of the refractive index. The orbitals polarize or distort as a result, with the degree of this varying depending on a constant (polarizability) specific to each material. Anions have a bigger effect than cations because they are more polarizable [44]. NBO is more likely to polarize than BO, this increase in glass polarizability was associated with changes in the borate glass structure because the formation of B_2O_3 resulted in the production of a significant number of (NBO) ions. It is well known that these NBOs are more polarizable than BOs in B_2O_2. Actually, the large number of NBOs points to an abundance of concentrated electrons that might act as a donor center in the glass network [54].

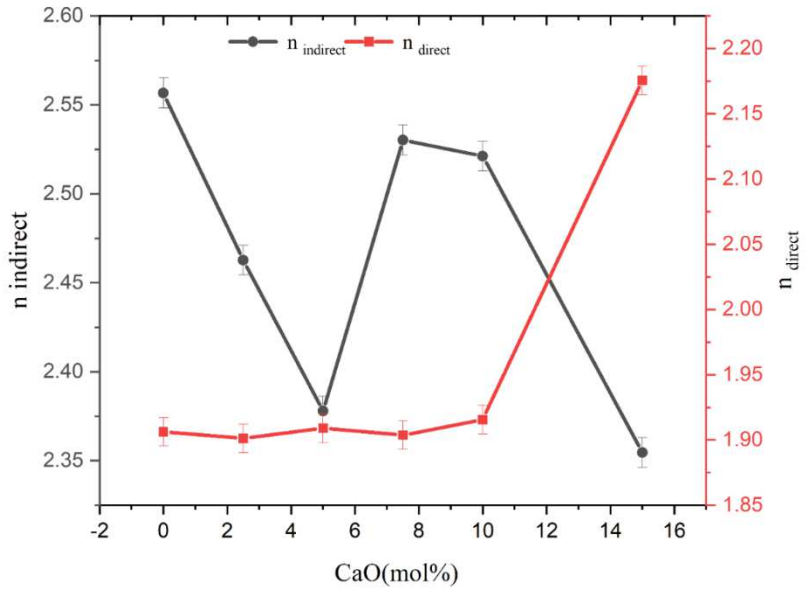

Figure 14: Variation of indirect and direct refractive indices of the glass samples as a function of CaO concentration.

The low refractive index is due to the low number of NBOs. More NBOs typically make objects more polarizing, which means they bend light more. When the number or arrangement of these modifiers varies, it causes changes in structure in some areas, which makes the refractive index uneven. As a result, the orbitals become polarized or change shape, and the amount of this change depends on a constant (polarizability) that is different for each material. The optical transmission numbers represent the percentage of waves that are transmitted, whereas the reflection loss shows the percentage of waves that are reflected. Figure 15 illustrates the variation in optical transmittance and

reflection loss of the prepared glasses as a function of CaO concentration, which is critical for optimizing bioactive glass performance in biomedical applications. The transmittance increases from 0.678 at 0 mol% CaO to a maximum of 0.719 at 15 mol%, indicating enhanced light penetration with CaO incorporation. Conversely, the reflection loss decreases from 0.193 to 0.163 over the same range, reflecting improved surface transparency and reduced light scattering. These optical improvements are beneficial for BG used in therapeutic windows or laser-assisted biomedical treatments, where high transparency and minimal reflectance enhance performance [56]. The modifications in optical behavior are attributed to structural changes in the glass matrix induced by CaO, which influences the refractive index and bonding environment, ultimately tailoring the glass for more efficient biomedical interaction.

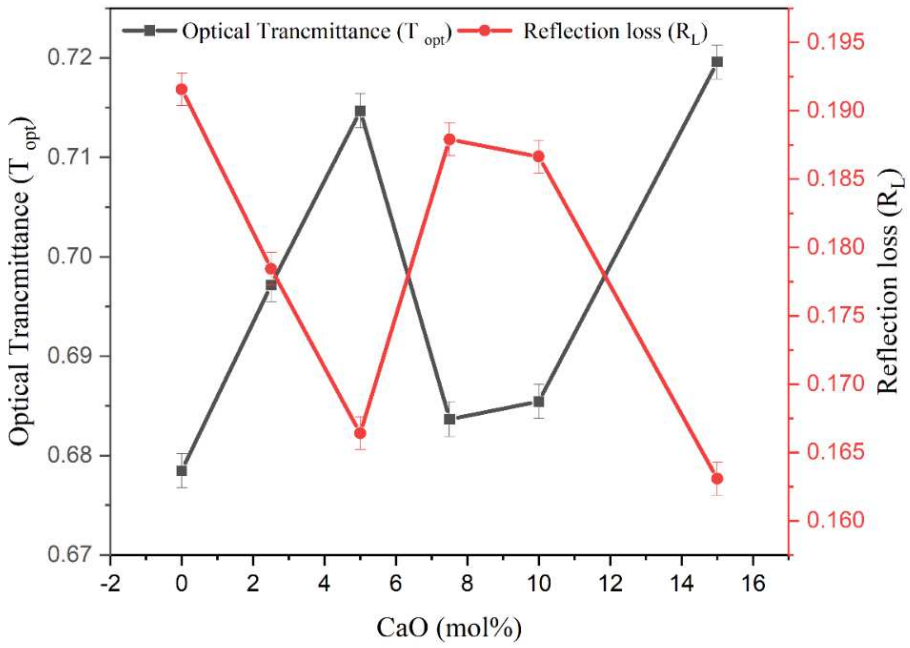

Figure 15: Variation of optical transmittance (T_{opt}) and reflection loss (R_L) as a function of CaO concentration in the glass matrix.

Table 6. refractive indices (n_{ind})($\pm$ **0.00843) and (** n_{dir})($\pm$ **0.01097)** , molar refractivity $R_m(cm)^3$, polarizability $\alpha_e(\times 10^{-24}cm^3)$, Optical transmittance (T_{opt} $\pm$0.00172), reflection loss(R_L $\pm$0.00119), metallization criterion (M$\pm$ 0.00193) and Optical basicity ($\mathbf{\Lambda}_{th}$ $\pm$ 0.00281)for different BPNC samples.

Parameters	Glass Code					
	BPNC0	BPNC1	BPNC2	BPNC3	BPNC4	BPNC5
n_{ind}	2.5567	2.4628	2.3779	2.5303	2.5212	2.3547
n_{dir}	1.9064	1.9012	1.909	1.9038	1.9156	2.1757
$R_m(cm)^3$	30.054	25.67	25.904	26.404	25.032	23.671
$\alpha_e \times 10^{-24}cm^3$	11.924	10.182	10.277	10.476	9.931	9.391
T_{opt}	0.67847	0.69715	0.71467	0.68365	0.68543	0.71959
R_L	0.19156	0.17845	0.1664	0.1879	0.18664	0.16307
M	0.35143	0.37197	0.39192	0.35705	0.359	0.39764
$\mathbf{\Lambda}_{th}$	0.6065	0.6195	0.6325	0.6455	0.6585	0.6845

3.3.3 Metallization criterion optical basicity

The metallization criteria is a theoretical technique that helps figure out how likely a material is to metallize and how well produced glasses insulate based on its band gap energy [57]. The Lorentz–Lorenz equation shows that the (R_M) and (V_m) are used to determine the (M) based on the refractive index [58] :

$$M = 1 - \frac{R_M}{V_M} \qquad (24)$$

Herzfeld came up with a hypothesis on how condensed matter behave as metal. He said that the refractive index becomes infinite when ${}^{R_M}/_{V_M} = 1$ in the Lorentz-Lorenz equation. The outcome implies that the glasses turn into metal and the electron moves about. Researchers think that materials with ${}^{R_M}/_{V_M}$ less than 1 are not metallic. On the other hand, materials with ${}^{R_M}/_{V_M}$ equal to or more than 1 have moving electrons, which means they are probably metallic.

Duffy and Ingram's equation, which describes the optical properties of the constituent oxides, is used to calculate the theoretical optical basicity (Λ_{th}) of the multicomponent glass. The theoretical or average optical basicity (Λ_{th}) denotes the theoretical or average optical basicity of the multicomponent glass system. It is calculated from the weighted contribution of each constituent oxide using their individual optical basicity values (Λ) and their molar fractions in the glass composition. Therefore, Λ_{th} reflects the overall electron-donating ability of oxide ions in the entire glass network rather than that of a single oxide [59].

$$\Lambda_{th} = \Lambda_1 X_1 + \Lambda_2 X_2 + \Lambda_3 X_3 + \cdots + \Lambda_n X_n \qquad (25)$$

Where $\Lambda_1 . \Lambda_2 . \Lambda_3 . \cdots . \Lambda_n$ in equation (25) represent the Λ_{th} of each oxide and $X_1 . X_2 . X_3 . \cdots . X_n$ stand for the equivalent fractions of each oxide in the glass system. Equation (25) reflects the average bulk basicity from all oxide species, including bridging and nonbridging. Theoretical Λ_{th} helps us figure out how efficiently oxygen in glass can give up electrons, which is analogous to how lasers function. Λ_{th} may also be used to measure the acid-base properties of molten salts, slags, alloys, glasses, and oxides [59].

A high optical basicity means that the oxide ions can give a lot of electrons to the cations. To find out how optically basic each oxide is, we use a basicity moderating factor (γ_i) that is based on Pauling electronegativity and Λ_{th} measurements for mixed glasses that rely on their composition [60].

$$\gamma_i = 1.36(\chi_i - 0.26) \qquad (26)$$

Where χ_i represents Pauling electronegativity.

The values of Pauling electronegativity (χ_i), Basicity Moderating (γ_i), and optical basicity (Λ) for each oxide are summarized in Table 7. These parameters provide insight into the electron-donating ability of the cations, which influences the glass network structure, bonding strength, and optical properties. Λ represents the optical basicity of an individual oxide, which is an intrinsic property of a pure oxide and is independent of the glass composition. It reflects the basic strength of an oxide when considered alone. The individual optical basicity mainly depends on the electronegativity of the cation bonded to oxygen; oxides containing cations with lower electronegativity exhibit higher optical basicity due to stronger electron-donating ability of O^{2-} ions. Figure 16 illustrates the variation of the (M) and (Λ) with increasing CaO content in the glass system. When you can see, the (Λ) goes down when more CaO is added. This drop shows that the glass network is becoming more acidic. The drop in (Λ) is linked to a decrease in the negative charge density on oxygen atoms, which makes it harder for them to give up electron density. Because of this, the cation-oxygen bonds become less covalent and more ionic [57]. The (M), which provides insight into the non-metallic nature of the material (values < 1 indicate insulating behavior), ranges from 0.351 at 0 mol% CaO to 0.398 at 15 mol% CaO. The highest value of M (0.397) is observed at 1.5 mol % CaO, after which it drops to 0.351 at 0 mol%, and then increases again. This fluctuation suggests changes in the electronic polarizability

and bonding character within the glass matrix. Simultaneously, the (Λ), which indicates the electron-donating ability of oxide ions in the glass, shows a steady rise from 0.6065 at 0 mol% CaO to 0.6845 at 15 mol% CaO. This consistent increase reflects the introduction of more basic oxide (CaO), which enhances the ionic nature of the glass and affects its reactivity and bonding environment. These trends are important for bioactive glass applications. A moderate (M) supports high electrical insulation, desirable for biomedical implants to prevent electrical interference in physiological environments. Meanwhile, increasing (Λ) promotes greater ion release (e.g., Ca^{2+}), a key factor in stimulating hydroxyapatite (HA) layer formation on glass surfaces, crucial for bone bonding and tissue regeneration [26] . Therefore, adjusting CaO concentration not only tunes the physical and optical properties but also optimizes the biological performance of the glass.

Table 7: Glass cations' basicity properties. Pauling electronegativity (χ_i), Basicity Moderating (γ_i), and optical basicity (Λ).

Code	χ_i	γ_i	$\Lambda = \gamma_i^{-1}$
B	2.04	2.4208	0.41308
P	2.19	2.6248	0.3809
Na	0.93	0.9112	1.0974
Ca	1	1.0064	0.9936

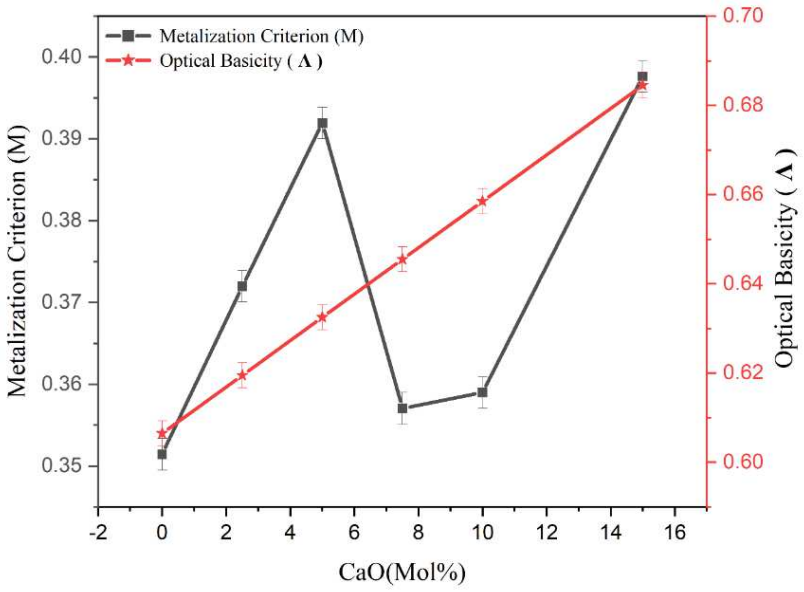

Figure 16: Variation of metallization criterion (M) and optical basicity (Λ) with CaO concentration in the glass system.

3.4 Differential Scanning Calorimetry/Thermogravimetric Analysis

The Differential Scanning Calorimetry/Thermogravimetric Analysis (DSC/TGA) thermograms of the $(65-x)B_2O_3$–$15P_2O_5$–$20Na_2O$–$xCaO$ glass system ($x = 0$–15 mol%) recorded from room temperature up to ~900 °C are shown in Figure 17. All compositions exhibit the typical thermal behavior of amorphous glasses, characterized by the appearance of a glass transition temperature (T_g), followed by an exothermic crystallization peak (T_c) and a high-temperature endothermic melting peak

(T_m), confirming the glassy nature of the prepared samples. The methods for obtaining T_g, T_c and T_m for the glass samples are illustrated in Figure 18 for sample BPNC0 and then the method is applied for the rest samples.

As observed in Figure 17 and summarized in Table 8, the glass transition temperature (T_g), identified from the baseline shift in the DSC/TGA curves, lies in the range of approximately 240.8 - 304.7 °C. T_g increased and decreased progressively with increasing CaO content. This fluctuation indicates that CaO plays a significant role on the rigidity of the glass network. The incorporation of Ca^{2+} ions, which possess a higher field strength than Na^{+} ions, leads to the formation of stronger Ca-O-B and Ca-O-P bonds. These stronger linkages restrict the mobility of the glass structural units, thereby increasing the temperature required for the onset of the glass transition [62]. At higher temperatures, the crystallization temperature (T_c) appears as a broad exothermic peak between 413.6-468.1°C, as clearly visible in Figure 17. The T_c values listed in Table 8 show a fluctuation between lower and higher temperatures with increasing CaO concentration. This behavior affects the resistance to crystallization, which can be attributed to the increased cross-link density and reduced mobility of non-bridging oxygens caused by CaO addition. The stabilization effect of Ca^{2+} ions suppress nucleation and crystal growth processes within the glass matrix [63]. The melting temperature (T_m), observed as a strong endothermic peak at temperatures ranging from 682.4 - 782.8 °C (Figure 17), also increased and decreased with CaO content, as reported in Table 8. This behavior in T_m reflects the strengthening and densification of the borophosphate glass network due to CaO incorporation, which enhances bond strength and structural compactness.

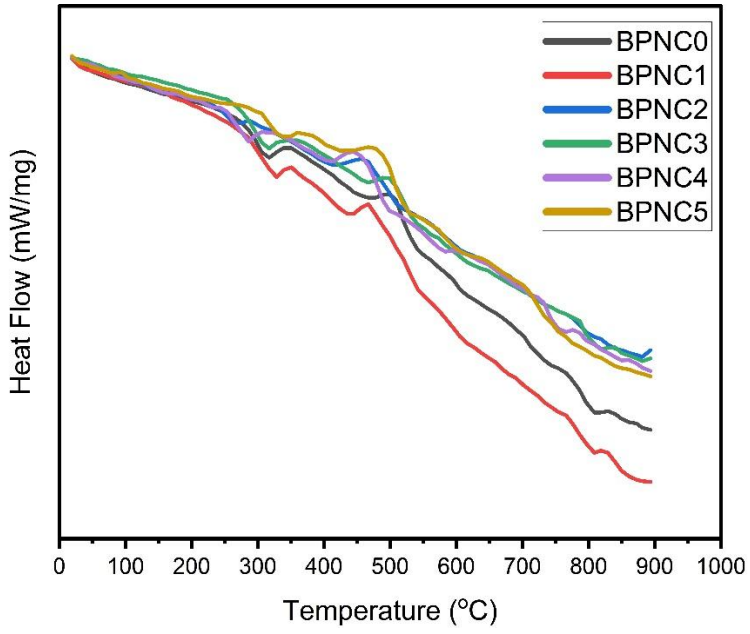

Figure 17: DSC/TGA thermogram for BPNC glass samples.

The thermal stability of the glass samples was evaluated using the stability parameter $\Delta T = T_c - T_g$, and the calculated values are presented in Table 8. The results show that the thermal stability (ΔT >100 °C) for all samples indicates improved glass-forming ability and higher resistance to devitrification and highest thermal stability of the glass. Glasses containing higher CaO concentrations 7.5 mol% exhibit the highest thermal stability, which is desirable for high-temperature processing and practical applications [63]. The glass-forming tendency of the prepared glasses was evaluated using the Hruby parameter (H_r), which is calculated from thermal analysis data according

to $H_r = \frac{T_c - T_g}{T_m - T_c}$. A higher H_r value indicates a wider supercooled liquid region and, consequently, a greater resistance to crystallization during heating, reflecting better glass-forming ability and higher thermal stability of the glass system [60]. In the present borophosphate glass series, the H_r values show a slight increasing trend with increasing CaO content, suggesting an enhancement in glass-forming tendency. This behavior can be attributed to the role of Ca^{2+} ions in strengthening the glass network through the formation of Ca-O bonds, which reduce structural rearrangement and hinder crystal nucleation. As a result, the incorporation of calcium improves the thermal stability and promotes the formation of a more stable glass structure [60-62].

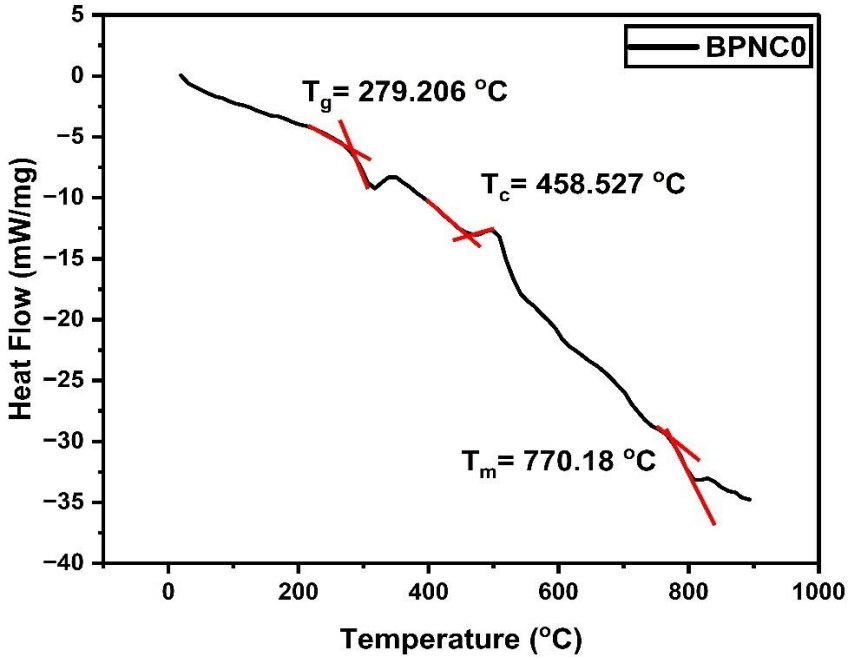

Figure 17: DSC/TGA thermogram for BPNC0 glass samples.

Table 8: Glass transition temperature (T_g), crystallization temperature (T_c) and melting temperature (T_m), thermal stability (ΔT) and glass forming tendency (H_r) for BPNC glass samples.

Sample	T_g/°C	T_c/ °C	T_m/ °C	$\Delta T = T_c - T_g$	$H_r = (T_c - T_g)/(T_m - T_c)$
BPNC0	279.2	458.5	770.1	179.3	0.575
BPNC1	282.4	434.9	774.2	152.4	0.449
BPNC2	240.8	415.6	682.4	174.8	0.655
BPNC3	262.1	469.1	782.8	206.9	0.659
BPNC4	253.6	413.6	731.6	160.1	0.503
BPNC5	304.7	430.6	706.1	125.9	0.457

4. Conclusion:

This study successfully synthesized and characterized a series of CaO-modified borophosphate-based glasses to evaluate their structural and optical behaviors for potential bioactive applications. XRD analysis confirmed the amorphous nature of all samples. FTIR analysis reveals that the introduction of CaO into BPNC0 significantly alters the vibrational spectra, promoting the formation of phosphate and borate linkages while modifying hydroxyl group interactions. Increased

CaO concentrations lead to the emergence of non-bridging oxygens and changes in bonding networks, indicating a transition from a more polymerized to a depolymerized glass structure. The physical parameters such as density and molar volume revealed significant trends: density increased from 2.163 to 2.532 g/cm^3 with CaO addition up to 7.5 mol%, then slightly decreased at higher concentrations, indicating structural compaction followed by network disruption. The molar volume showed an inverse trend, decreasing with increased density, confirming that CaO acted as a network modifier, (but in 15%CaO will become 39.293 g/cm^3) filling interstitial spaces and influencing the glass compactness. Further, the (OMV) fluctuated from 15.98 cm³/mol at 0 mol% CaO to 14.34 cm³/mol at 15 mol% CaO, indicating a denser oxygen environment within the glass matrix. In contrast, the (OPD) increased from 62.58 to 69.73 by changing CaO concentration range. This trend reflects tighter atomic packing and enhanced network connectivity, contributing to better mechanical stability and chemical durability essential traits for bioactive glass performance in physiological environments. Additionally, the polaron radius (R_p) exhibited a slight decrease from 1.2 Å to 0.66 Å, while the internuclear distance (R_i) reduced from reduced 3.005 Å to 1.632 Å as CaO content increased. These reductions suggest a more compact structural arrangement and subtle shifts in electronic cloud overlap, which can affect charge transport, ionic conductivity, and ultimately influence the bioactivity and degradation behavior of the glass in biological systems. The detailed optical investigations revealed composition-dependent trends in bandgap energy, refractive index, Urbach energy, and optical basicity. The indirect bandgap (E_{ind}) varied nonlinearly with CaO content, increasing to a maximum of 3.16 eV at 15 mol% CaO, while the direct bandgap (E_{dir}) showed a notable increase at the highest CaO concentration at 5.71 eV at 2.5 mol%. The Urbach energy fluctuated (from 1.691 eV to 0.503 eV) and fluctuated steepness parameter (from 2.4 to 8.169) by increasing CaO levels indicated a reduction in disorder and enhanced structural stability. These changes corresponded to improved optical properties, such as increased transmittance (up to 0.72) reduced reflection loss (down to 0.678), which are advantageous for biomedical transparency. Moreover, the (M) remained below the critical threshold ($M < 0.5$), confirming the insulating nature of the glass system. A steady increase in (Λ) (from 0.6065 to 0.6845) suggests a greater ionic character, which is known to enhance bioactivity through improved ion release and bone bonding capabilities. These findings demonstrate that controlled CaO incorporation into borophosphate glass systems significantly tailors their optical and structural properties. T_g, T_c, and T_m increased and decreased depending on the CaO content indicating CaO acts as a network stabilizer, increasing rigidity and thermal resistance. The composition with 7.5 mol% CaO exhibits the highest thermal stability, suitable for high-temperature applications. The combination of high optical transmittance, tunable bandgap, improved stability, and increased optical basicity make these glasses strong candidates for bioactive applications, particularly in bone regeneration, implant coatings, and therapeutic delivery platforms.

Acknowledgment
We would like to express our deepest gratitude to Salahaddin University-Erbil for providing the opportunity and academic support to conduct this research.

Declarations Competing interests
We declare that we have no competing interests, or other interests that might be perceived to influence the results and/or discussion reported in this paper.

Funding
No funding was obtained for this study

Availability of data and materials
Most of the data supporting the findings of this study are available in the paper and the rest of the data sets generated during the current study are available from the corresponding author on reasonable request.

Author Contribution Statement:
Design, and analysis, interpretation of results, study conception and writing-review & editing: Saman Q. Mawlud
Methodology, data collection, study conception and writing the draft version: Gailan A. Saber

References

[1] Kargozar, S., et al., Bioactive glasses and glass/polymer composites for neuroregeneration: should we be hopeful? Applied Sciences, 2020. **10**(10): p. 3421.
[2] Sreena, R., et al., Bioactive Glass-Polymer Nanocomposites: A comprehensive Review on Unveiling its Biomedical Applications. Journal of Materials Chemistry B, 2024.
[3] Al-Harbi, N., et al., Silica-based bioactive glasses and their applications in hard tissue regeneration: A review. Pharmaceuticals, 2021. **14**(2): p. 75.
[4] Haider, A., et al., Strontium-and zinc-containing bioactive glass and alginates scaffolds. Bioengineering, 2020. **7**(1): p. 10.
[5] Zhang, Y., et al., Strontium-incorporated mesoporous bioactive glass scaffolds stimulating in vitro proliferation and differentiation of bone marrow stromal cells and in vivo regeneration of osteoporotic bone defects. Journal of Materials Chemistry B, 2013. **1**(41): p. 5711-5722.
[6] Gómez-Cerezo, M.N., et al., Multiscale porosity in mesoporous bioglass 3D-printed scaffolds for bone regeneration. Materials Science and Engineering: C, 2021. **120**: p. 111706.
[7] Sharifianjazi, F., et al., Advances in zinc-containing bioactive glasses: a comprehensive review. Journal of Functional Biomaterials, 2024. **15**(9): p. 258.
[8] Fu, Q., et al., Silicate, borosilicate, and borate bioactive glass scaffolds with controllable degradation rate for bone tissue engineering applications. I. Preparation and in vitro degradation. Journal of biomedical materials research part A, 2010. **95**(1): p. 164-171.
[9] Brown, R.F., et al., Growth and differentiation of osteoblastic cells on 13–93 bioactive glass fibers and scaffolds. Acta Biomaterialia, 2008. **4**(2): p. 387-396.
[10] Rahaman, M.N., et al., Bioactive glass in tissue engineering. Acta biomaterialia, 2011. **7**(6): p. 2355-2373.
[11] Abodunrin, O.D., K. El Mabrouk, and M. Bricha, A review on borate bioactive glasses (BBG): effect of doping elements, degradation, and applications. Journal of Materials Chemistry B, 2023. **11**(5): p. 955-973.
[12] Negut, I. and C. Ristoscu, Bioactive glasses for soft and hard tissue healing applications—A short review. Applied sciences, 2023. **13**(10): p. 6151.
[13] Rau, J.V., et al., Borate and silicate bioactive glass coatings prepared by nanosecond pulsed laser deposition. Coatings, 2020. **10**(11): p. 1105.
[14] Mawlud, S.Q., et al., Investigation of mechanical and chemical durability properties of oxide modifiers incorporated tellurite glass: ternary oxide glass. Ceramics International, 2025.
[15] Mahraz, Z.A.S., et al., Spectroscopic investigations of near-infrared emission from Nd3+-doped zinc-phosphate glasses: Judd-Ofelt evaluation. Journal of Non-Crystalline Solids, 2019. **509**: p. 106-114.
[16] Wenning, M. and S. Scherer, Identification of microorganisms by FTIR spectroscopy: perspectives and limitations of the method. Applied microbiology and biotechnology, 2013. **97**: p. 7111-7120.
[17] Khalil, E., et al., Mechanical properties, in vitro and in vivo bioactivity assessment of Na2O-CaO-P2O5-B2O3-SiO2 glass-ceramics. Ceramics International, 2018. **44**(7): p. 7867-7876.
[18] Prasad, S., et al., Elucidating the effect of CaF2 on structure, biocompatibility and antibacterial properties of S53P4 glass. Journal of Alloys and Compounds, 2020. **831**: p. 154704.
[19] Ren, M., et al., Preparation and chemical stability of CaO–P2O5–Na2O–B2O3 porous glass ceramics. Journal of non-crystalline solids, 2013. **380**: p. 78-85.

[20] Abo-Naf, S.M., et al., In vitro bioactivity evaluation, mechanical properties and microstructural characterization of Na2O–CaO–B2O3–P2O5 glasses. Spectrochimica Acta Part A: Molecular and Biomolecular Spectroscopy, 2015. **144**: p. 88-98.
[21] Krishnamacharyulu, N., et al., An in-vitro bioactive, structural and degradation studies on B2O3–SiO2–P2O5–Na2O–CaO glass system incorporated with chromium ions. Materials Today: Proceedings, 2018. **5**(13): p. 26280-26289.
[22] Krishnamacharyulu, N., et al., Investigation on silver doped B2O3–SiO2–P2O5–Na2O–CaO bioglass system for biomedical applications. Journal of Alloys and Compounds, 2018. **734**: p. 318-328.
[23] Mohamed, A.F. and S.Q. Mawlud, Effect of zinc oxide on structural and optical properties borotellurite glass: ternary glass. Zanco Journal of Pure and Applied Sciences, 2023. **35**(4): p. 14-21.
[24] Hench, L.L., Bioceramics: from concept to clinic. Journal of the american ceramic society, 1991. **74**(7): p. 1487-1510.
[25] Brauer, D.S., Bioactive glasses—structure and properties. Angewandte Chemie International Edition, 2015. **54**(14): p. 4160-4181.
[26] Jones, J.R., Review of bioactive glass: from Hench to hybrids. Acta biomaterialia, 2013. **9**(1): p. 4457-4486.
[27] Singh, D. and G.P. Singh, Conversion of covalent to ionic behavior of Fe2O3–CeO2–PbO–B2O3 glasses for ionic and photonic application. Journal of alloys and compounds, 2013. **546**: p. 224-228.
[28] Dawaud, R.S.E.S., et al., Optical and structural properties of lithium sodium borate glasses doped Dy3+ ions. Journal of Molecular Structure, 2014. **1075**: p. 113-117.
[29] Rao, A.S., et al., Spectroscopic studies of Nd3+-doped alkali fluoroborophosphate glasses. Optical Materials, 1998. **10**(4): p. 245-252.
[30] Umar, S., et al., Physical, structural and optical properties of erbium doped rice husk silicate borotellurite (Er-doped RHSBT) glasses. Journal of Non-Crystalline Solids, 2017. **472**: p. 31-38.
[31] Reticcioli, M., et al., Small polarons in transition metal oxides. Handbook of Materials Modeling: Applications: Current and Emerging Materials, 2020: p. 1035-1073.
[32] Emin, D., Polarons in condensed matter. arXiv preprint arXiv:2205.02878, 2022.
[33] Acharya, A., et al., Charge carrier transport and electrochemical stability of Li2O doped glassy ceramics. Materials Science and Engineering: B, 2020. **260**: p. 114612.
[34] Al-Ghamdi, H., et al., Effect of PbO and B2O3 on the physical, structural, and radiation shielding Properties of PbO-TeO2-MgO-Na2O-B2O3 glasses. Sustainability, 2022. **14**(15): p. 9695.
[35] Hussein, K.I., et al., The effect of ZnO, MgO, TiO2, and Na2O modifiers on the physical, optical, and radiation shielding properties of a TeTaNb glass system. Materials, 2022. **15**(5): p. 1844.
[36] Yadav, A.K. and P. Singh, A review of the structures of oxide glasses by Raman spectroscopy. RSC advances, 2015. **5**(83): p. 67583-67609.
[37] Babu, M.M., et al., Structural and in vitro bioactivity of phosphate-based glasses for bone regeneration, in Advances in Glass Research. 2023, Springer. p. 113-152.
[38] Upender, G., et al., Structural and optical studies of quaternary glass system. Advanced Materials Letters, 2022. **13**(2): p. 2202-1695.
[39] Farouk, M., et al., Optical absorption and structural studies of bismuth borate glasses containing Er3+ ions. Journal of non-crystalline solids, 2013. **371**: p. 14-21.
[40] El-Deen, L.S., M.S. Al Salhi, and M.M. Elkholy, IR and UV spectral studies for rare earths-doped tellurite glasses. Journal of Alloys and Compounds, 2008. **465**(1-2): p. 333-339.
[41] Mawlud, S.Q., Optical properties of tellurite glasses embedded with gold nanoparticles. Tellurite glass smart materials: applications in optics and beyond, 2018: p. 105-142.
[42] Ansari, S.A., et al., Concentration dependent improved spectroscopic characteristics and near white light emission in boro phosphate glasses doped with holmium. Applied Sciences, 2022. **12**(5): p. 2632.

[43] Chen, Y., et al., A study of nonlinear optical properties in Bi2O3–WO3–TeO2 glasses. Journal of Non-Crystalline Solids, 2008. **354**(29): p. 3468-3472.
[44] Tafida, R., et al., Optical Basicity and Electronic Polarisability of Zinc Tellurite Glass System Doped with Sm 3 ions.
[45] Ahmed, K.F., et al., Physical and optical properties of zinc tellurite Glass embedded Silver Nanoparticles co-dopedwith Nd3+/Er3+ ions. Sulaimani Journal for Pure and Applied Sciences, 2017. **19**(1): p. 149-158.
[46] Mawlud, S.Q., et al., Optical absorption spectra of samarium doped TeO2-Na2O glasses. Solid State Science and Technology, 2016. **24**(2): p. 94-106.
[47] Tauc, J., 1968. Optical properties and electronic structure of amorphous Ge and Si. *Materials research bulletin*, *3*(1), pp.37-46.
[48] Mott, N.F. and Davis, E.A., 2012. *Electronic processes in non-crystalline materials*. OUP Oxford.
[49] Aghababaei, H., Faeghinia, A. and Soleimani, F., 2025. Novel phosphate glass ceramic of CaO-TiO2-P2O5 system containing Nd3+. *Ceramics International*.
[50] Sendova, M. and Jiménez, J.A., 2021. Band gap analysis and correlation with glass structure in phosphate glasses melted with various allotropes of carbon. *Chemical Physics*, *547*, p.111207.
[51] Magdas, D.A., Vedeanu, N.S. and Toloman, D., 2015. Study on the effect of vanadium oxide in calcium phosphate glasses by Raman, IR and UV–vis spectroscopy. *Journal of Non-Crystalline Solids*, *428*, pp.151-155.
[52] Taha, T.A. and Rammah, Y.S., 2016. Optical characterization of new borate glass doped with titanium oxide. *Journal of Materials Science: Materials in Electronics*, *27*(2), pp.1384-1390.
[53] Wahab, E.A., et al., Basicity, electronegativity, optical parameters and radiation attenuation characteristics of P2O5-As2O3-PbO glasses doped vanadium ions. Journal of Inorganic and Organometallic Polymers and Materials, 2022. **32**(10): p. 3983-3996.
[54] Ahmed, A.A. and S.Q. Mawlud, Physical and optical properties of ternary lead-bismuth tellurite glass. Heliyon, 2023. **9**(6).
[55] Kumari, S., S. Yadav, and D. Mohan, Nonlinear optical characterization of zinc doped tellurite glasses for optical limiting performance. Optik, 2021. **228**: p. 166193.
[56] Kaur, G., et al., A review of bioactive glasses: their structure, properties, fabrication and apatite formation. Journal of Biomedical Materials Research Part A: An Official Journal of The Society for Biomaterials, The Japanese Society for Biomaterials, and The Australian Society for Biomaterials and the Korean Society for Biomaterials, 2014. **102**(1): p. 254-274.
[57] Halimah, M., et al., Optical basicity and electronic polarizability of zinc borotellurite glass doped La3+ ions. Results in physics, 2017. **7**: p. 581-589.
[58] Elazoumi, S., et al., Effect of PbO on optical properties of tellurite glass. Results in physics, 2018. **8**: p. 16-25.
[59] Duffy, J. and M.D. Ingram, An interpretation of glass chemistry in terms of the optical basicity concept. Journal of Non-Crystalline Solids, 1976. **21**(3): p. 373-410.
[60] SANJAY, KISHORE, N., AGARWAL, A., DAHIYA, S., PAL, I. and KUMAR, N., 2013. Optical and Spectroscopic Studies of Fe2O3-Bi2O3-B2O3: V2O5 Glasses. *Modern Physics Letters B*, *27*(28), p.1350207.
[61] Kaky, K.M., et al., Structural, thermal and optical absorption features of heavy metal oxides doped tellurite rich glasses. Results in Physics, 2017. **7**: p. 166-174.
[62] Chauhan, S., Bala, R., Gaur, S. and Rani, S., 2022. Effect of Bi2O3 on structural and optical properties of Li2O· PbO· Bi2O3· B2O3 glasses. *Journal of Materials Science: Materials in Electronics*, *33*(29), pp.22835-22850.
[63] Yadav, D., Bala, R., Chauhan, S. and Gaur, S., 2025. Structural and optical investigations of lithium-modified lead bismuth borate glasses. *Solid State Communications*, *399*, p.115859.

Supplementary Files

This is a list of supplementary files associated with this preprint. Click to download.

- SupplementaryFile.xlsx